Journal of Magnetic Resonance 303 (2019) 28–41

Contents lists available at ScienceDirect

Journal of Magnetic Resonance

journal homepage: www.elsevier.com/locate/jmr

Evaluation of excitation schemes for indirect detection of ^{14}N *via* solid-state HMQC NMR experiments

Andrew G.M. Rankin [a,*], Julien Trébosc [a,b], Piotr Paluch [a,c], Olivier Lafon [a,d], Jean-Paul Amoureux [a,e,*]

[a] Univ. Lille, CNRS, Centrale Lille, ENSCL, Univ. Artois, UMR 8181 – UCCS – Unit of Catalysis and Chemistry of Solids, F-59000 Lille, France
[b] Univ. Lille, CNRS-FR2638, Fédération Chevreul, F-59000 Lille, France
[c] Centre of Molecular and Macromolecular Studies, Polish Academy of Sciences, Sienkiewicza 112, PL-90363 Lodz, Poland
[d] Institut Universitaire de France, 1 rue Descartes, F-75231 Paris Cedex 05, France
[e] Bruker Biospin, 34 rue de l'industrie, F-67166 Wissembourg, France

ARTICLE INFO

Article history:
Received 10 January 2019
Revised 3 April 2019
Accepted 4 April 2019
Available online 5 April 2019

Keywords:
Solid-state NMR
D-HMQC
J-HMQC
^{14}N
Selective excitation
SLP
DANTE
XiX

ABSTRACT

It has previously been shown that ^{14}N NMR spectra can be reliably obtained through indirect detection *via* HMQC experiments. This method exploits the transfer of coherence between single-(SQ) or double-quantum (DQ) ^{14}N coherences, and SQ coherences of a suitable spin-1/2 'spy' nucleus, e.g., ^{1}H. It must be noted that SQ-SQ methods require a carefully optimized setup to minimize the broadening related to the first-order quadrupole interaction (i.e., an extremely well-adjusted magic angle and a highly stable spinning speed), whereas DQ-SQ ones do not. In this work, the efficiencies of four ^{14}N excitation schemes (DANTE, XiX, Hard Pulse (HP), and Selective Long Pulse (SLP)) are compared using *J*-HMQC based numerical simulations and either SQ-SQ or DQ-SQ ^{1}H-{^{14}N} *D*-HMQC experiments on L-histidine HCl and N-acetyl-L-valine at 18.8 T and 62.5 kHz MAS. The results demonstrate that both DANTE and SLP provide a more efficient ^{14}N excitation profile than XiX and HP. Furthermore, it is shown that the SLP scheme: (i) is efficient over a large range of quadrupole interaction, (ii) is highly robust to offset and rf-pulse length and amplitude, and (iii) is very simple to set up. These factors make SLP ideally suited to widespread, non-specialist use in solid-state NMR analyses of nitrogen-containing materials.

1. Introduction

Nitrogen atoms are ubiquitous in biomolecules, *e.g.*, DNA and proteins, and organic, hybrid and inorganic materials, such as pharmaceuticals, polyamides, functionalized silica, metal-organic frameworks or nitrides. However, the NMR observation of the two nitrogen isotopes, ^{15}N and ^{14}N, remains challenging owing to their unfavorable NMR properties.

1.1. ^{15}N

It is a spin-1/2 nucleus, which often leads to high-resolution spectra, even for solids. However, owing to its very low natural abundance (NA = 0.36%) and its low gyromagnetic ratio, $\gamma_{15N} \approx 0.1\gamma_{1H}$, a major limitation of ^{15}N NMR is often the lack of sensitivity. This issue can be circumvented by ^{15}N isotopic enrichment, but this approach can be costly, time-consuming and difficult to achieve. Alternative methods to enhance the NMR sensitivity and detect the ^{15}N signals in natural abundance consists of the use of (i) indirect detection *via* protons at high Magic Angle Spinning (MAS) frequencies using through-space or through-bond ^{1}H → ^{15}N polarization transfers [1,2] or (ii) dynamic nuclear polarization enhanced ^{1}H → ^{15}N cross-polarization under MAS (CPMAS) experiments [2,3].

1.2. ^{14}N

Conversely, the ^{14}N isotope has two major advantages: (i) a very high natural abundance (NA = 99.64%), and (ii) the fact that the knowledge of the quadrupole interaction of this spin-1 nucleus provides additional information about the local environment of nitrogen atoms.

1.2.1. Direct detection

The direct NMR detection of ^{14}N nuclei is challenging for several reasons [4–6]. First, it has a spin-1 value and hence no central

* Corresponding authors at: Univ. Lille, CNRS, Centrale Lille, ENSCL, Univ. Artois, UMR 8181 – UCCS – Unit of Catalysis and Chemistry of Solids, F-59000 Lille, France (J.-P. Amoureux).
E-mail addresses: andrew.rankin@univ-lille.fr (A.G.M. Rankin), jean-paul.amoureux@univ-lille.fr (J.-P. Amoureux).

https://doi.org/10.1016/j.jmr.2019.04.004
1090-7807/

transition between energy levels m_N = ±1/2. For a powdered sample, the signal of the two single-quantum transitions, $^{14}N^{SQ}$, between energy levels m_N = 0 and ±1 is broadened by the first-order quadrupole interaction (H_{Q1}) over a width of $3C_Q/2$, where C_Q is the quadrupolar coupling constant. For this isotope, a value of C_Q = 7 MHz has been reported [7], which corresponds to a powder pattern width of 10.5 MHz. This large line broadening severely decreases the sensitivity since the total integrated intensity is spread over a broad spectral width. Second, the sensitivity of directly-detected spectra being proportional to $\gamma^{3/2}$ that of ^{14}N isotope is further decreased with respect to ^{15}N by its low gyromagnetic ratio with $\gamma_{14N} \approx 0.072\gamma_{1H}$. Third, the pulse dead-times, which are inversely proportional to γ, are thus long for ^{14}N nuclei, whereas the broad linewidths result in short Free-Induction Decays (FID). This combination also decreases the sensitivity of ^{14}N direct detection. For ^{15}N isotope, this issue can be circumvented by the use of a spin-echo sequence or the CPMG (Carr-Purcell Meiboom-Gill) variant, which improves the sensitivity by the acquisition of a train of echoes in every scan [8]. However, these methods are not easy to use for the ^{14}N isotope, because π-pulses are difficult to implement for this spin-1 nucleus. Forth, an additional difficulty for the direct ^{14}N detection is the need to excite a broad spectral width, which can exceed the excitation bandwidth of the radio-frequency (rf) pulses and the detection bandwidth of the probe. This limitation is exacerbated for ^{14}N isotope because the rf-fields are proportional to γ, which is small for ^{14}N. When the width of the $^{14}N^{SQ}$ spectrum exceeds the detection bandwidth of the probe or the excitation bandwidth of the pulses, sub-spectra with different frequency offsets are acquired and then co-added to generate the full wide powder pattern [8]. This piecewise acquisition technique is called VOCS (Variable Offset Cumulative Spectrum). It has been shown that the excitation bandwidth of directly detected ^{14}N experiments can be increased using adiabatic pulses, such as WURST (wideband uniform-rate smooth-truncation) under static conditions [9] or trains of short rotor-synchronized rf-pulses in the manner of DANTE (Delays Alternating with Nutation for Tailored Excitation) under MAS conditions [10–12]. The sensitivity of directly detected ^{14}N experiments under static conditions can be further enhanced by an initial polarization transfer from protons using BRAIN-CP (broadband adiabatic inversion cross-polarization) [13].

Nevertheless, a major limitation of the direct $^{14}N^{SQ}$ detection under static conditions is the lack of resolution since this signal is broadened by H_{Q1} and the powder patterns of distinct nitrogen sites extensively overlap. Hence, this approach is only suitable for samples with one or two nitrogen sites. MAS can improve the resolution of $^{14}N^{SQ}$ spectra, but these experiments require a very precise adjustment and a high stability of the MAS frequency and angle [14–17]. The resolution can be improved by the detection of the ^{14}N double-quantum ($^{14}N^{DQ}$) coherences between energy levels m_N = ±1 since these coherences are only broadened by the second-order quadrupole interaction (H_{Q2}). These coherences can be directly excited and acquired at twice the ^{14}N Larmor frequency with the overtone sequence. This type of direct excitation has been reported first under static conditions [18,19] and more recently under MAS [4,20,21]. The detection of this usually "forbidden" DQ transition is allowed by a perturbation of the Zeeman spin states by the large quadrupole interaction. The sensitivity of overtone experiments can be enhanced by $^1H \rightarrow {}^{14}N$ CPMAS transfer and DNP [22,23]. However, the overtone ^{14}N direct excitation and detection experiments are usually less sensitive than the direct detection of $^{14}N^{SQ}$ transitions. Furthermore, the slow nutation of the overtone signal results in a small excitation bandwidth, which may prevent the detection of distinct nitrogen sites. WURST pulses can improve the overtone excitation bandwidth, but they decrease the sensitivity [24].

1.2.2. Indirect detection

For protonated samples, the lack of resolution and sensitivity of direct ^{14}N detection can be partially overcome by the indirect detection of $^{14}N^{SQ}$ or $^{14}N^{DQ}$ transitions *via* protons, denoted ^1H-{$^{14}N^{SQ}$} and ^1H-{$^{14}N^{DQ}$} respectively [5,25–27], using two-dimensional (2D) experiments at high MAS frequencies, such as HMQC (heteronuclear multiple-quantum correlation) [25,28], HSQC (heteronuclear single-quantum correlation) [29,30], double cross-polarization [31], or sequences using ^{14}N rf-irradiation lasting hundreds of microseconds to generate ^1H-^{14}N multiple-quantum coherences [32]. It has been shown that the HSQC sequence is less sensitive than the HMQC one [29,33]. Furthermore, for HMQC experiments, coherence transfers *via* ^1H-^{14}N dipolar interactions, which are reintroduced by the application of heteronuclear dipolar recoupling schemes, such as $SR4_1^2$ [34], in dipolar-mediated HMQC schemes, are usually faster and more efficient than coherence transfers *via* a combination of *J*-coupling and second-order quadrupolar-dipolar cross-terms, also known as residual dipolar splitting, during the free evolution periods of the conventional *J*-mediated HMQC (*J*-HMQC) scheme [28,35]. For ^1H-{$^{14}N^{SQ}$} HMQC experiments, the broadening of $^{14}N^{SQ}$ transitions due to the first-order quadrupole interaction is refocused by the rotor synchronization of the indirect evolution period, *i.e.*, $t_1 = nT_R$.

As for the ^{14}N direct detection, a challenge for the indirect detection is the creation of ^{14}N coherences because the magnitude of H_{Q1} exceeds that of the rf-field by several orders of magnitude. In ^1H-{^{14}N} HMQC experiments, ^{14}N SQ and DQ coherences have been created and reconverted by: short 'hard' pulses (HP) using high rf-power [36,37], sideband selective long pulses (SLP) [25,28,35,38,39], and DANTE trains [10,40]. Recently, single-sideband XiX (X inverse X) pulse trains have also been used in the ^1H-{$^{14}N^{DQ}$} HMQC sequence [41]. These four excitation schemes (HP, SLP, DANTE and XiX) have all been applied at the ^{14}N Larmor frequency. ^1H-{$^{14}N^{DQ}$} *D*-HMQC 2D spectra have also been recorded using overtone irradiation at twice the ^{14}N Larmor frequency, in the manner of rectangular, WURST and composite pulses [42–44]. Nevertheless, it has been reported that ^1H-{$^{14}N^{DQ}$} *D*-HMQC experiments on amino-acids using rectangular pulses or DANTE trains at the ^{14}N Larmor frequency, or overtone pulses are less sensitive than the ^1H-{$^{14}N^{SQ}$} *D*-HMQC ones using rectangular pulses or DANTE trains [35,39,45]. Furthermore, for the γ polymorph of glycine, we have shown that the ^1H-{$^{14}N^{SQ}$} *D*-HMQC experiment using DANTE is slightly more sensitive, but less robust to offset, than its SLP variant [39,40]. The performances of ^1H-{$^{14}N^{DQ}$} *D*-HMQC using XiX excitation have not been compared to those of the other existing ^1H-{^{14}N} *D*-HMQC schemes.

Here, we compare the performances of ^1H-{^{14}N} *D*-HMQC experiments using HP, SLP, DANTE and XiX schemes, all at the ^{14}N Larmor frequency. These sequences are first described using an average Hamiltonian theory. We then analyze the efficiency of these experiments and their robustness to offset, rf-field inhomogeneity and quadrupole interaction. The performances of ^1H-{^{14}N} *D*-HMQC schemes using HP, SLP and DANTE schemes are also assessed by experiments on L-histidine. HCl and N-acetyl-L-valine, denoted His and NAV hereafter, respectively.

2. Pulse sequences and theory

Fig. 1 shows the ^1H-{^{14}N} *J*- and *D*-HMQC sequences using rectangular pulses (HP or SLP), the basic D_1^K DANTE, and the XiX schemes for the excitation and the reconversion of ^{14}N coherences evolving during the t_1 period. In the *J*-HMQC sequence, the defocusing and refocusing delays, denoted τ_J, are free evolution periods. In the *D*-HMQC sequence, the $SR4_1^2$ recoupling was applied during the defocusing and refocusing delays, τ_D, in order to reintroduce

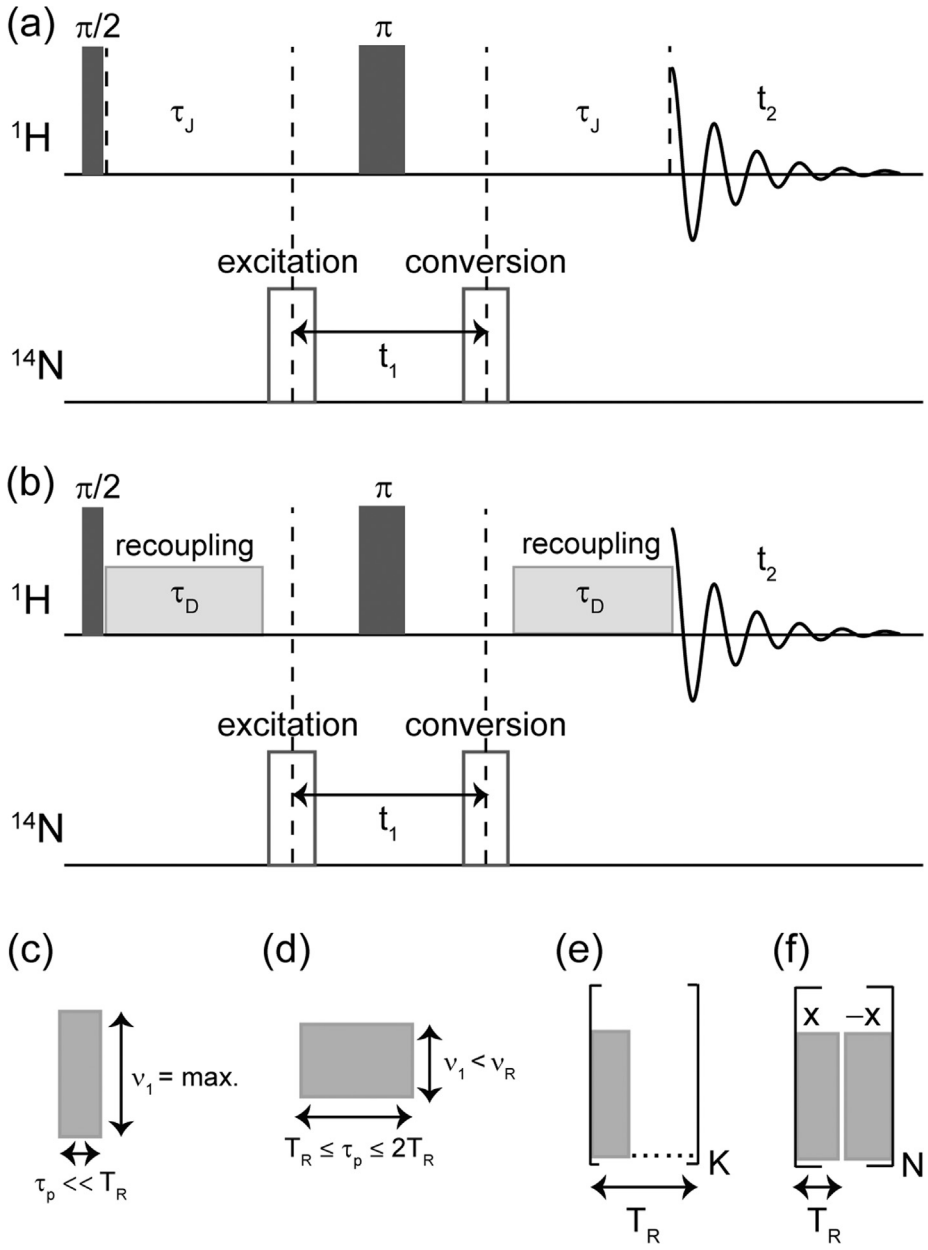

Fig. 1. ^{1}H-{^{14}N} (a) *J*- and (b) *D*-HMQC sequences using for the excitation and reconversion of ^{14}N coherences in place of the open rectangles in (b) on the ^{14}N channel: (c) HP, (d) SLP, (e) D_1^K and (f) XiX schemes. The t_1 period is defined as the delay between the middles of the excitation and reconversion blocks.

the ^{1}H-^{14}N dipolar couplings. During $SR4_1^2$, the ^{1}H rf-field is equal to twice the MAS frequency: $\nu_1 = 2\nu_R$. This recoupling reintroduces the space component $|m| = 1$ of the ^{1}H-^{14}N dipolar couplings and ^{1}H chemical shift anisotropy (CSA), whereas it suppresses the ^{1}H-^{1}H dipolar couplings, the ^{1}H isotropic chemical shifts and the hetero-nuclear *J*-couplings with protons. As the $SR4_1^2$ scheme is non-γ-encoded, the beginning of the two $SR4_1^2$ periods in the *D*-HMQC sequence must be separated by an integer number of rotor periods.

For ^{1}H-{^{14}N} HMQC experiments, the ^{1}H *x*-magnetization created by the first pulse evolves during the defocusing period into [40,46]

$$S_x\left(\frac{1+2\cos(2\omega_{HN}\tau)}{3}\right)+S_xQ_z\left(\frac{\cos(2\omega_{HN}\tau)-1}{3}\right)+S_yI_z\sin(2\omega_{HN}\tau) \quad (1)$$

where S_xQ_z is the *x*-magnetization of proton, leading to a triplet with intensities 1:−2:1 for the coupling with ^{14}N nucleus, S_yI_z is the *y*-magnetization of proton, leading to a triplet with intensities 1:0:−1. The angular frequency ω_{HN} is equal to πJ_{HN} for *J*-HMQC and to $\omega_{D,HN}$ for *D*-HMQC:

$$\omega_{D,HN}=\frac{1}{4}b_{HN}\sin^2\left(\beta_{PR}^{D,HN}\right)\cos(2\varphi) \quad (2)$$

with

$$\varphi=\gamma_{PR}^{D,HN}+\alpha_{RL}^{0}-\omega_R t^0 \quad (3)$$

In Eqs. (2) and (3), b_{HN} denotes the dipolar coupling constant in rad s^{-1}, the Euler angles $\left\{0,\beta_{PR}^{D,HN},\gamma_{PR}^{D,HN}\right\}$ relate the inter-nuclear ^{1}H-^{14}N direction to the MAS rotor-fixed frame, and t^0 refers to the starting time of the symmetry-based scheme. The subsequent evolution of the density matrix depends on the used excitation scheme.

2.1. HP

HP can achieve the uniform excitation of ^{14}N powder patterns provided its length τ_p is sufficiently short [39,40]

$$\tau_p < 2/(3\pi C_Q). \quad (4)$$

For $C_Q = 1$ MHz, Eq. (4) indicates that the uniform excitation requires $\tau_p < 0.2$ μs. The maximal ^{14}N rf-field compatible with the specifications of a 1.3 mm double-resonance MAS probe is $\nu_1 \approx 100$ kHz, which results in a flip angle of $\theta < 2\pi\nu_1\tau_p \approx 8°$. This maximum value is much smaller than the optimal angles, $\theta \approx 54.4$ and 90°, yielding maximal transfer efficiency for ^{1}H-{^{14}N^{SQ}} and ^{1}H-{^{14}N^{DQ}} *D*-HMQC experiments, respectively [40]. These small tilt angles decrease the efficiency of ^{1}H-{^{14}N} HMQC experiments using HP. When Eq. (4) is satisfied, the evolution under H_{Q1} during τ_p is negligible and the Hamiltonian in the jolting-frame during HP is equal to [39,41]

$$\tilde{H} = 2\pi\nu_1 I_x \quad (5)$$

In Eq. (1), a HP corresponding to this Hamiltonian converts I_z into I_y and the quadrupolar order operator Q_z into K_y and D_x operators, which represent respectively the ^{14}N^{SQ} coherences along y-axis antiphase with respect to H_{Q1} and the ^{14}N^{DQ} coherences along the x-axis. After the first HP, only the signal resulting from either S_xK_y and S_yI_y or S_xD_x operator is detected, according to ^{1}H-{^{14}N^{SQ}} or ^{1}H-{^{14}N^{DQ}} HMQC experiment is used, respectively. The coherences evolve under isotropic shift during t_1. For ^{1}H-{^{14}N^{SQ}}, the excitation and reconversion HPs must be rotor-synchronized in order to refocus the evolution under H_{Q1} during t_1. In that case, it has been shown [40] that the signal is proportional to

$$S(\tau) \propto \frac{2}{3}\sin^2(\theta)\langle\sin^2(2\omega_{HN}\tau)\rangle + \frac{2}{3}\sin^2(2\theta)\langle\sin^4(\omega_{HN}\tau)\rangle \quad (6)$$

where $\langle\cdots\rangle$ denotes the powder average, and for ^{1}H-{^{14}N^{DQ}} it is proportional to

$$S(\tau) \propto \frac{2}{3}\sin^4(\theta)\langle\sin^4(\omega_{HN}\tau)\rangle \quad (7)$$

For *J*-HMQC experiments, $\omega_{HN} = \pi J_{HN}$, and with HP the maximal transfer efficiency is obtained for $\theta = \pi/2$ and a delay of

$$\tau = 1/(4J_{HN}) \text{ for } ^1\text{H} - \left\{^{14}\text{N}^{SQ}\right\} \text{ or } 1/(2J_{HN}) \text{ for } ^1\text{H} - \left\{^{14}\text{N}^{DQ}\right\} \quad (8)$$

This is contrary to *J*-HMQC experiments with a pair of two spin-1/2 nuclei, where the optimum signal is always observed for $\tau = 1/(2J)$.

2.2. D_1^K

^{14}N SQ and DQ coherences in ^{1}H-{^{14}N} HMQC experiments can also be created using rotor-synchronized DANTE schemes, denoted D_M^K, which consist of a train of rectangular pulses of length, τ_p, rf-amplitude, ν_1, with identical phases. The length of a D_M^K train is equal to KT_R and *M* equally spaced pulses are applied during each of these *K* rotor periods. The D_M^K schemes with $M = 1$ and $M \geq 2$ are referred to as basic and interleaved DANTE sequences, respectively [10–12]. The DANTE excitation profile in the frequency domain consists of a comb of rf-spikelets, all separated from the carrier frequency by a multiple of $M\nu_R$, with amplitude decreasing with the separation from the carrier frequency according to a sinc function. For a D_1^K scheme resonant with the center-band and with individual pulses satisfying Eq. (4), the first-order average Hamiltonian can be written as [40,47]

$$\bar{H} = 2\pi\nu_1\tau_p I_x/T_R \quad (9)$$

This equation is only valid when the evolution under H_{Q2} is negligible during KT_R. As the magnitude of H_{Q2} is proportional to $C_Q^2/\nu_{0,14N}$, for large C_Q values this assumption requires high B_0 field and MAS frequencies, which limit the losses due to H_{Q2} during D_1^K [40]. When Eq. (9) is valid and the excitation and reconversion of D_1^K schemes are rotor-synchronized, *i.e.*, separated by an integer multiple of rotor periods, the signals of ^{1}H-{^{14}N^{SQ}} and ^{1}H-{^{14}N^{DQ}} HMQC experiments using DANTE schemes are given by Eqs. (6) and (7), respectively, where $\theta = 2\pi K\nu_1\tau_p$, and the optimum delays by Eq. (8). In a first approximation, the D_1^K train can hence be viewed as a HP with an effective rf-field of $K\nu_1$. If S_{FWHM} denotes the offset width of each excitation **S**pikelet, and E_{FWHM} that of the global **E**nvelope excitation, then these values are equal to [40]

$$S_{FWHM} \approx 1.1/KT_R; \quad E_{FWHM} \approx 1.1/\tau_p \quad (10)$$

In order to obtain an excitation profile that is robust with respect to the offset, S_{FWHM} must be large and hence K must be small. This implies that most of the time, except when the isotropic frequency range, $\Delta\nu_{14N,iso}$, is small, the largest possible rf-field should be used. It is common that several different ^{14}N species exist in the same sample, all with different C_Q values and isotropic resonances, $\nu_{14N,iso}$. Therefore, as a starting point for the experimental optimization, the number of rotor periods should accommodate the isotropic frequency range, and the individual pulse length should excite the majority of the static linewidth for the maximum C_Q value

$$K \approx 1/(T_R * \Delta\nu_{14N,iso}) \text{ and } \tau_p \leq 0.6/C_{Q,max} \quad (11)$$

However, these simple rules are mainly applicable in the case of weak H_{Q2} effects, as discussed later.

It has been shown (i) that ^{1}H-{^{14}N^{DQ}} HMQC experiments are less efficient than the ^{1}H-{^{14}N^{SQ}} ones, and (ii) that HMQC with D_1^K is more efficient than with D_M^K ($M > 1$) [39,40,45]. For these reasons, we only studied here ^{1}H-{^{14}N^{SQ}} HMQC sequences using D_1^K trains.

2.3. SLP

The HP scheme is based on the assumption of a simultaneous excitation of all crystallites, which is why the maximum possible rf-field strength is then used. Recently, another scheme has been proposed, based on the rotor-driven sequential excitation of the crystallites, which occurs when the time-dependent quadrupole interaction becomes small as a result of sample rotation [39]. This principle leads to the use of selective long pulses (SLP). It must be noted that the name of SLP may appear to be misleading because, as we will see below, this pulse is robust towards offsets (Figs. 6 and 12). This is contrary to the way SLP are used in liquids. However, in MAS NMR it has very recently been demonstrated that, contrary to HP and D_1^K pulses that excite numerous sidebands, SLP only excites the sideband that coincides with the carrier frequency (Figs. 9d and 14d in [59]). As a result, SLP can be considered as selective when only observing the sideband combs. The relatively high efficiency of SLP comes from the fact that all crystallites in the rotor provide a signal, which always occurs when their interaction frequency matches that of the carrier irradiation due to sample rotation. This is contrary to HP and D_1^K excitations, where a large part of the sample gives a small signal due to rf-inhomogeneity. As a consequence, the SLP signal is always at the spinning sideband that is the closest to the carrier frequency, not at the isotropic chemical shift, as shown in Fig. 9d in [59]. The selective excitation of a single spinning sideband of the ^{14}N^{SQ} spectrum requires a sufficiently long pulse with low rf-amplitude: $\tau_p > T_R$ and $\nu_1 < \nu_R$. We employed here rectangular pulses satisfying these conditions. The evolution of the density operator between

time points separated by several rotor periods can be described by an average Hamiltonian. For a SLP with phase ϕ_p and resonant with the center-band of the $^{14}N^{SQ}$ spectrum, its first-order value is given by [41]

$$\overline{H}^{(1)} = 2\pi\nu_1 A_0 R_z(\phi_p) U_Q(\xi_0)^{-1} I_x U_Q(\xi_0) R_z(\phi_p)^{-1} \quad (12)$$

A_0 and ξ_0 are the intensity and the phase of the center-band of the $^{14}N^{SQ}$ spinning sideband manifold. A_0 does not depend on the γ_{PR} Euler angle specifying the orientation of the electric field gradient tensor with respect to the rotor-fixed frame, but depends on the two other Euler angles $\{\alpha_{PR}, \beta_{PR}\}$. The scaling of the rf-field strength by A_0 stems from the fact that the instantaneous resonance frequency of the nucleus changes rapidly during the pulse and hence the rf-field rotates the magnetization only during a part of the pulse. R_z (ϕ_p) is the rotation operator of the ^{14}N spin about the z-axis through angle ϕ_p and U_Q (ξ_0) is the quadrupolar propagator defined as:

$$U_Q(\xi_0) = \exp\left[-i\xi_0 \frac{Q_z}{3}\right] \quad (13)$$

When considering only the Hamiltonian given by Eq. (12) during SLP, it can be shown that the ^{1}H-{$^{14}N^{SQ}$} HMQC signal is proportional to

$$S(\tau) \propto \frac{2}{3}\langle \sin^2(\theta)\sin^2(2\omega_{HN}\tau)\rangle + \frac{2}{3}\langle \sin^2(2\theta)\sin^4(\omega_{HN}\tau)\rangle \quad (14)$$

and that of ^{1}H-{$^{14}N^{DQ}$} to

$$S(\tau) \propto \frac{2}{3}\langle \sin^4(\theta)\sin^4(\omega_{HN}\tau)\rangle \quad (15)$$

where $\theta = 2\pi A_0 \nu_1 \tau_p$ depends on the Euler angles $\{\alpha_{PR}, \beta_{PR}\}$ through A_0.

Furthermore, for a SLP with a phase ϕ_p and resonant with the center-band of the $^{14}N^{SQ}$ spectrum, the second-order average Hamiltonian is given by [41]

$$\overline{H}^{(2)} = \frac{\pi\nu_1^2}{2\nu_R} d\left[Q_z + R_z(\phi_p) D_x R_z(\phi_p)^{-1}\right] \quad (16)$$

with

$$d = \sum_{p=-\infty, p\neq 0}^{+\infty} \frac{A_p^2 - A_{-p}^2 - 2A_p A_0 \cos(\xi_p - \xi_0) + 2A_{-p} A_0 \cos(\xi_{-p} - \xi_0)}{p} \quad (17)$$

where A_p and ξ_p denote the intensity and the phase of the $^{14}N^{SQ}$ p^{th}-order spinning sideband manifold. In Eq. (16), $\overline{H}^{(2)}$contains Q_z and D_x terms, which commute [46]. The latter can convert the I_z operator in Eq.1 into D_y one, which represents the $^{14}N^{DQ}$ coherences along the y-axis [39] and hence, this term contributes to the signal of ^{1}H-{$^{14}N^{DQ}$} HMQC. However, the double-quantum term of $\overline{H}^{(2)}$ in Eq. (16) does not commute with $\overline{H}^{(1)}$, which can thus perturb the creation of $^{14}N^{DQ}$ coherences in ^{1}H-{$^{14}N^{DQ}$} HMQC experiments, by creating unwanted $^{14}N^{SQ}$ coherences.

2.4. XiX

This issue can be circumvented by the use of the XiX scheme, which is constructed as a train of 2N SLP pulses of the same length T_R, with alternating phase x and $-x$ to eliminate $\overline{H}^{(1)}$ [41]. For XiX scheme resonant with the center-band, $\overline{H}^{(2)}$ is given by Eq. (16) with $\phi_p = 0$ and the signal of ^{1}H-{$^{14}N^{DQ}$} HMQC is equal to

$$S(\tau) \propto \frac{2}{3}\langle \sin^2(\theta)\sin^2(2\omega_{HN}\tau)\rangle \quad (18)$$

with $\theta = 2\pi Nd(\nu_1/\nu_R)^2$ [41]. Hence, for ^{1}H-{$^{14}N^{DQ}$} J-HMQC experiments using XiX schemes, the maximal transfer efficiency is achieved for

$$\tau = 1/(4J_{HN}) \quad (19)$$

3. 1D numerical simulations

3.1. Simulation parameters

The spin dynamics during the aforementioned pulse sequences were simulated using SIMPSON software [48]. The powder average was calculated using 3864 $\{\alpha_{MR}, \beta_{MR}, \gamma_{MR}\}$ Euler angles that described the orientation of the molecule in the rotor frame. The 966 $\{\alpha_{MR}, \beta_{MR}\}$ pairs were selected according to the REPULSION algorithm [49], whereas the four γ_{MR} angles were regularly stepped from 0 to 360°. The simulations were performed for one isolated ^{1}H-^{14}N spin pair. The ^{14}N nucleus was subject to H_{Q1} and H_{Q2} with $\{C_Q$ (MHz), $\eta_Q\}$ = {1.18, 0.5} or {3.21, 0.32}, which result in powder patterns with a full width of 1.77 and 4.82 MHz, respectively. For a powder-averaged resonance, two effects are related to H_{Q2}, both proportional to $C_Q^2/\nu_{0,14N}$: a crystallite dependent shift which leads to a second-order broadening, and an overall positive quadrupole induced shift (QIS) of the gravity center

$$\nu_{QIS} = (3 + \eta_Q^2) C_Q^2 / (40\nu_{0,14N}) \quad (20)$$

At B_0 = 18.8 T, ν_{QIS} = 1957 and 13827 Hz, for the two previous cases with C_Q = 1.18 and 3.21 MHz, respectively. The former parameters correspond to those of ^{14}N nucleus of α-glycine [15,50] and are typical of those measured in amino acids. The latter correspond to those of N-acetyl-L-valine (NAV) [51]. Except in Fig. S4, no CSA was introduced because the magnitude of this interaction is often negligible with respect to the quadrupole one [52,53]. In order to decrease the computing time, the simulations were done with the J-HMQC sequence shown in Fig. 1a, instead of the targeted D-HMQC one (Fig. 1b). This, however, does not change the analysis of the efficiency of the ^{14}N excitation and reconversion, which is the main topic of this article. Therefore, in the simulations performed at B_0 = 18.8 T with ν_R = 62.5 kHz, ^{1}H and ^{14}N nuclei were only scalar coupled with $J_{1H\text{-}14N}$ = 400 Hz.

We simulated the 1D signals of ^{1}H-{$^{14}N^{SQ}$} J-HMQC sequences using HP, SLP, D_1^K and XiX schemes as well as ^{1}H-{$^{14}N^{DQ}$} J-HMQC sequences using SLP and XiX schemes. The rf-field for the π/2 and π-pulses on the ^{1}H channel was fixed to $\nu_{1,1H}$ = 100 kHz and was always applied on-resonance. Except in Fig. 6, the pulses on ^{14}N channel were applied on resonance, i.e., their carrier frequency was equal to the sum of the isotropic chemical shift and the QIS. The maximum rf-field on ^{14}N channel did not exceed 200 kHz in order to be consistent with the rf-power specifications of common MAS probes. For ^{1}H-{$^{14}N^{SQ}$} J-HMQC simulations, the delays were set to their shortest optimal value of $\tau_J = 1/(4J_{HN})$ = 2.5 ms (Eq. (8)). For ^{1}H-{$^{14}N^{DQ}$} simulations, we employed $\tau_J = 1/(4J_{HN})$ for XiX (Eq. (19)) and $\tau_J = 1/(2J_{HN})$ for SLP (Eq. (8)). For these 1D simulations, the t_1 delay was fixed to an integer multiple of T_R, in order to refocus the evolution under H_{Q1}. For HP and SLP, $t_1 = 2T_R$, which is the largest τ_p value used in the simulations. For the same reason, t_1 was fixed to KT_R and $2NT_R$ for D_1^K and XiX schemes, respectively. In all J-HMQC simulations, the transfer efficiency was normalized with respect to the ^{1}H signal observed with an ideal spin-echo experiment with Dirac pulses. The maximum efficiency of ^{1}H-{$^{14}N^{SQ}$} J-HMQC using two ideal Dirac ^{14}N π/2-pulses for one ^{1}H-^{14}N spin pair with C_Q = 0 is equal to 0.35. This ideal value will be used as a benchmark in the following discussion.

3.2. Optimal rf-field amplitude and duration

The simulation-based analysis started by calculating a series of two-dimensional maps showing the transfer efficiency *versus* the rf-field and the duration of excitation and reconversion schemes applied to ^{14}N channel on-resonance. In the case of HP or SLP these maps are displayed as (ν_1 *vs.* τ_p), whereas for XiX, they are displayed as (ν_1 *vs.* N). In the case of D_1^K, each (ν_1, τ_p) map was calculated for one particular *K* value. The maps corresponding to the best efficiencies are shown either in the main text (Figs. 2–5) or in the supplementary information (Figs. S1 and S2).

As seen in Fig. 2a, the maximal efficiency for ^{1}H-{$^{14}N^{SQ}$} *J*-HMQC using HP is achieved for τ_p = 0.75 μs and ν_1 = 200 kHz, which corresponds to θ = 54°. This angle is lower than 90°. Furthermore, τ_p = 0.75 μs does not satisfy Eq.4 for glycine and hence, HP does not produce a uniform excitation of the $^{14}N^{SQ}$ powder pattern. Therefore, the efficiency of the sequence only reaches 0.2, which is 40% smaller than that of ^{1}H-{$^{14}N^{SQ}$} *J*-HMQC sequence using Dirac pulses for a ^{14}N nucleus not subject to quadrupole interaction. As seen in Fig. 2b, the efficiency is further decreased for larger C_Q.

For ^{1}H-{$^{14}N^{SQ}$} *J*-HMQC using SLP (Fig. 3a and c), the maximal transfer efficiency is obtained for $\tau_p \approx 2T_R$ and it reaches 0.23 with $\nu_1 \approx$ 35 kHz for glycine and 0.20 with $\nu_1 \approx$ 50 kHz for NAV. Those efficiencies are *ca.* the same and 100% higher than those obtained for glycine and NAV, respectively, using HP with ν_1 = 200 kHz. These results indicate that (i) SLP is more efficient than HP for the excitation and the reconversion of $^{14}N^{SQ}$ coherences, notably for ^{14}N nuclei subject to large quadrupole interaction, and (ii) SLP requires much lower rf-field than HP. For ^{1}H-{$^{14}N^{DQ}$} *J*-HMQC using SLP, maximal transfer efficiencies are obtained under similar conditions than for ^{1}H-{$^{14}N^{SQ}$} (Fig. 3b and d). However, the excitation and the reconversion of $^{14}N^{DQ}$ coherences are significantly less efficient than those of $^{14}N^{SQ}$ ones.

For ^{1}H-{$^{14}N^{SQ}$} *J*-HMQC using D_1^5 applied to glycine, a maximal efficiency of 0.32 is obtained for rf-fields down to ν_1 = 80 kHz. For such rf-field, the optimal τ_p length is 0.6 μs, which corresponds to $\theta \approx$ 86°. This angle is close to the theoretical optimal angle of 90°, whereas the achieved efficiency reaches almost the theoretical one of 0.35. This high efficiency indicates small losses due to H_{Q2}. For NAV, ^{1}H-{$^{14}N^{SQ}$} *J*-HMQC with D_1^6 yields a maximal efficiency of 0.21 for $\tau_p \approx$ 0.3 μs and ν_1 = 100 kHz, *i.e.*, $\theta \approx$ 65°. The reduced efficiency and tilt angle stem from faster H_{Q2} dephasings for NAV than glycine since H_{Q2} is proportional to C_Q^2. As a simple rule, when H_{Q2} dephasings are small, $T_R\nu_{QIS} \leq 0.05$ (e.g. 0.032 for glycine), the optimal total pulse duration corresponds to $\theta \approx 90°$, but it decreases when it is not the case (*e.g.* 0.22 for NAV).

The simulations showing the simulated efficiency of ^{1}H-{$^{14}N^{SQ}$} *J*-HMQC with D_1^K scheme and $3 \leq K \leq 8$ for a spin system corresponding to glycine or NAV are shown in the Supplementary Information (Fig. S1 or S2, respectively). Practically, the D_1^K optimization is performed by fixing ν_1 at its maximum value (80 kHz with our MAS probe), and by optimizing τ_p for various *K* values.

Fig. 5b shows that maximal efficiency for ^{1}H-{$^{14}N^{DQ}$} *J*-HMQC with XiX is obtained for ν_1 = 30 kHz and N = 4 for glycine. For NAV, the maximal efficiency is obtained for smaller *N* values because of losses due to H_{Q2} (Fig. 5d). Furthermore, for both glycine and NAV, XiX results in 45% lower efficiency for ^{1}H-{$^{14}N^{DQ}$} *J*-HMQC than with SLP. Fig. 5a and c indicate that XiX can also be used to excite and reconvert the $^{14}N^{SQ}$ coherences. Shorter *N* values are required for NAV in order to limit the losses produced by H_{Q2}. ^{1}H-{$^{14}N^{SQ}$} *J*-HMQC using XiX are twice less efficient than those using SLP for glycine and NAV.

The optimum parameters obtained from the aforementioned maps, as well as their resulting normalized efficiencies, Eff, are summarized in Table 1. These parameters were used in subsequent simulations. No further discussion of the XiX results will be presented in the remainder of this article, because their simulated and experimental efficiency and robustness (not shown) were consistently found to be much smaller than those of the SLP and D_1^K schemes.

3.3. Robustness

3.3.1. Offset

In addition to the on-resonance sensitivity, another important criterion is the robustness to offset, which is shown in Fig. 6a for glycine and Fig. 6b for NAV. The two most robust excitations are those related to SLP. Their widths are the same with SQ or DQ selection and they depend very little upon the C_Q value ($S_{FWHM} \approx$ 40 kHz). The D_1^K scheme is less robust ($S_{FWHM} \approx$ 20 kHz), and this value is the same for glycine and NAV. These results indicate that the robustness to offset mainly depends on the length of the excitation and reconversion blocks (see S_{FWHM} in Eq. (10)). The shorter

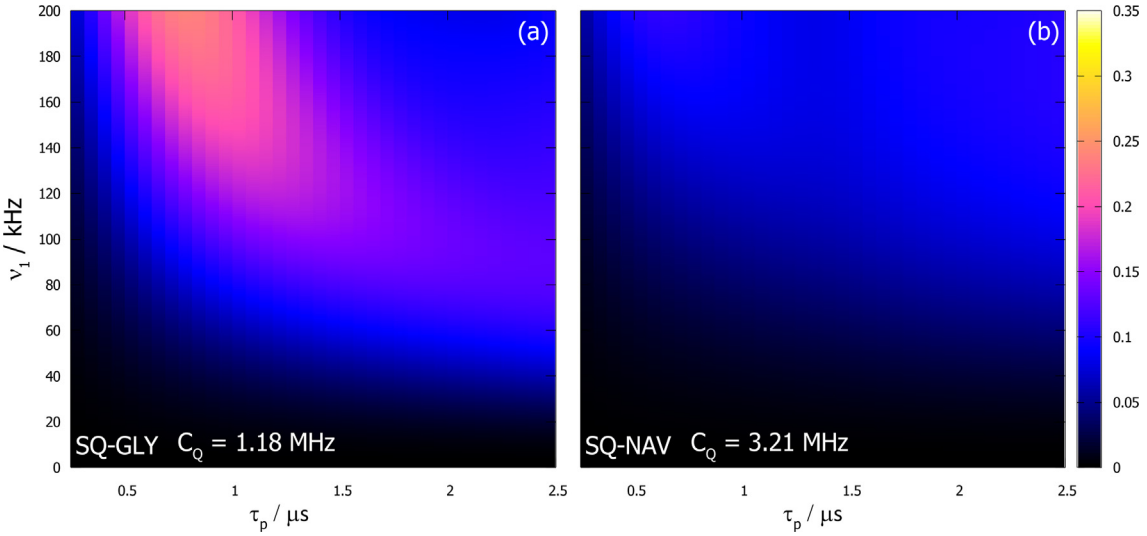

Fig. 2. Simulated on-resonance efficiency of ^{1}H-{$^{14}N^{SQ}$} *J*-HMQC sequence using HP *versus* τ_p and ν_1 for spin systems corresponding to (a) glycine and (b) NAV.

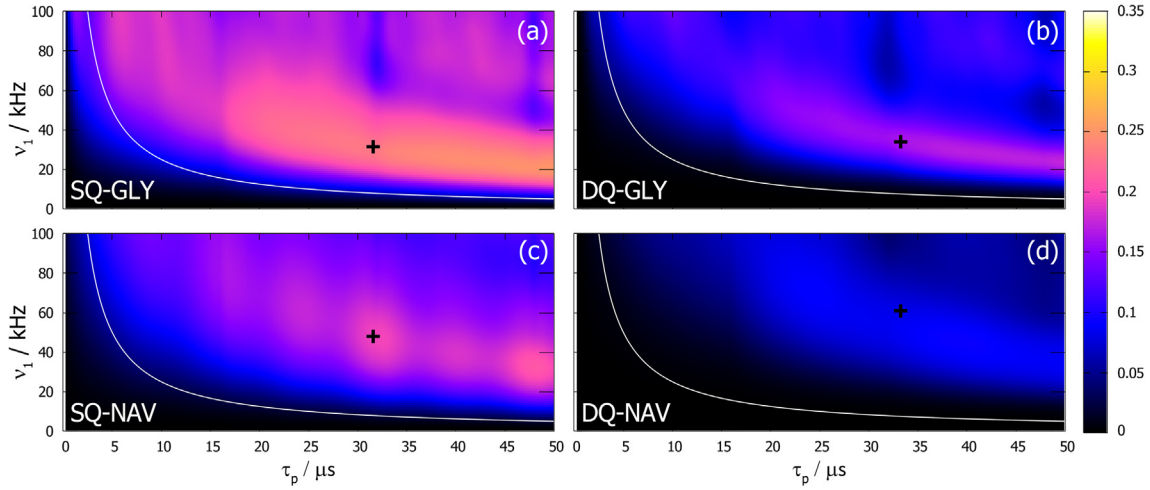

Fig. 3. Simulated on-resonance efficiency of (a and c) ^{1}H-{^{14}N^{SQ}} and (b and d) ^{1}H-{^{14}N^{DQ}} *J*-HMQC sequence using SLP *versus* τ_p and ν_1 for spin systems corresponding to (a and b) glycine and (c and d) NAV. The τ_p and ν_1 values corresponding to $\pi/2$-pulses are plotted as solid white lines.

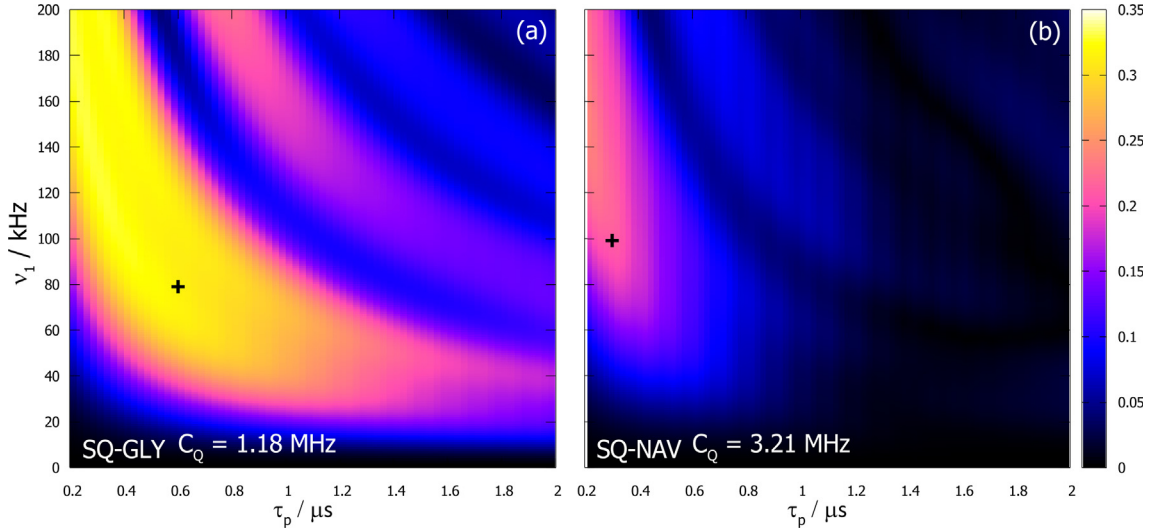

Fig. 4. Simulated on-resonance efficiency of ^{1}H-{^{14}N^{SQ}} *J*-HMQC sequence using D_1^K *versus* τ_p and ν_1 for spin systems corresponding to (a) glycine with $K = 5$ and (b) NAV with $K = 6$.

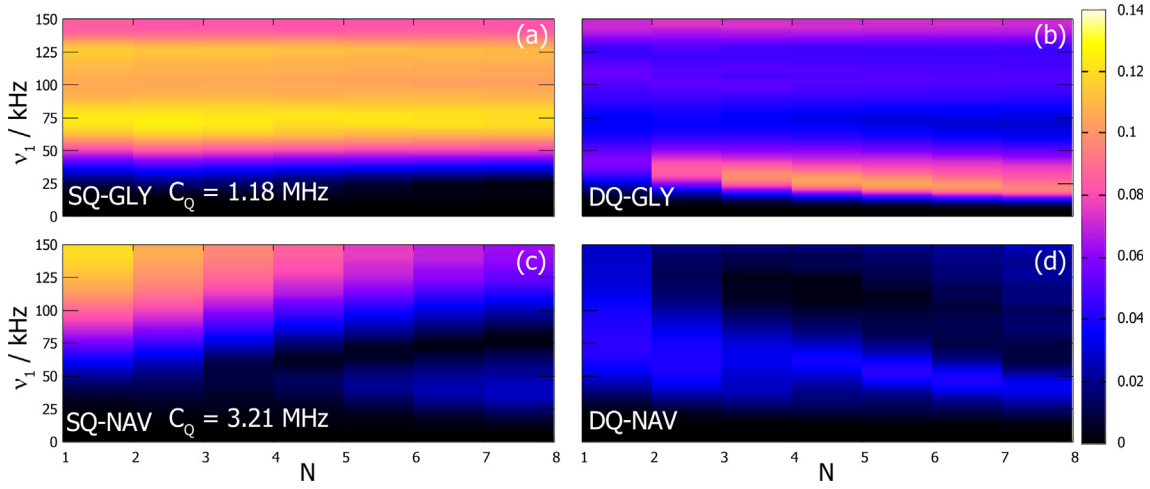

Fig. 5. Simulated on-resonance efficiency of (a and c) ^{1}H-{^{14}N^{SQ}} and (b and d) ^{1}H-{^{14}N^{DQ}} *J*-HMQC sequence using XiX *versus* *N* and ν_1 for spin systems corresponding to (a and b) glycine and (c and d) NAV.

Table 1
Optimum on-resonance simulation parameters used for glycine or NAV.

Excitation	τ_J	τ_p/μs	ν_1/kHz	Eff
Glycine				
HP SQ	1/4J	0.75	200	0.24
SLP SQ	1/4J	32 ($2T_R$)	30	0.23
SLP DQ	1/2J	32 ($2T_R$)	35	0.16
XiX SQ	1/4J	64 (N = 2)	75	0.13
XiX DQ	1/4J	128 (N = 4)	30	0.11
D_1^K SQ	1/4J	0.5 (K = 5)	80	0.32
NAV				
HP SQ	1/4J	0.75	200	0.11
SLP SQ	1/4J	32 ($2T_R$)	50	0.20
SLP DQ	1/2J	32 ($2T_R$)	55	0.10
XiX SQ	1/4J	32 (N = 1)	140	0.13
XiX DQ	1/4J	64 (N = 2)	65	0.05
D_1^K SQ	1/4J	0.3 (K = 6)	100	0.21

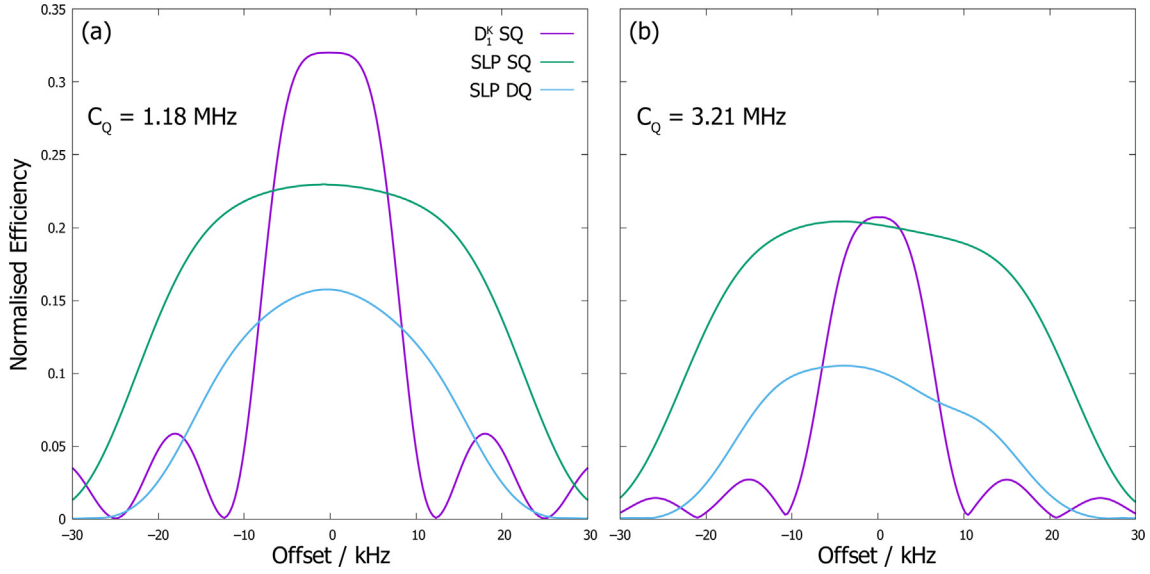

Fig. 6. Simulated efficiency of ^{1}H-{$^{14}N^{SQ}$} and ^{1}H-{$^{14}N^{DQ}$} *J*-HMQC sequences using SLP and ^{1}H-{$^{14}N^{SQ}$} with D_1^K with respect to ^{14}N offset for spin systems corresponding to (a) glycine and (b) NAV. The rf parameters (ν_1, τ_p) are indicated with + on Figs. 2–4.

length of SLP with respect to D_1^K explains the higher robustness to offset of the former.

3.3.2. Rf-inhomogeneity

Previous simulations were performed with one particular rf-field. However, there exists an inherent distribution of rf-fields in the coil of NMR probes, mostly along the axis of the solenoid coil in MAS probes. Typically, this amplitude is maximal at the center of the coil and it drops by *ca.* 50% near the edges [54–57].

For SLP, the simulations displayed in Fig. 7 show that, independently of the C_Q value, (i) the optimal rf-field is equal to *ca.* 50–80% of ν_R, and (ii) the relative widths of these curves, *i.e.,* the FWHM divided by the optimum rf-field, which are the relevant values with respect to rf-inhomogeneity, are approximately the same with SQ or DQ selection.

With D_1^K trains, the rf-requirement is higher than with SLP, but the efficiency is larger with small C_Q values. Conversely for large C_Q values, the losses due to H_{Q2} decrease the efficiency.

3.3.3. Spinning speed and CSA

The robustness with respect to spinning speed and CSA (Figs. S3 and S4, respectively) was also tested. The simulations show that SLP depends little upon these two parameters, but that D_1^K is sensitive with respect to spinning speed fluctuations. However, modern MAS speed controllers can provide sufficiently stable MAS frequency to allow the use of D_1^K schemes.

3.3.4. Quadrupole interaction

The last aspect analyzed *via* simulations was the robustness with respect to the C_Q value. This is an important criterion as this parameter can vary between 0 and 7 MHz, depending on the local environment of ^{14}N nucleus [5,7]. To that end, the optimum efficiency of the two most efficient methods, SLP and D_1^K with SQ selection, was calculated for a series of quadrupole parameters corresponding to C_Q = 0–4 MHz. These simulations were performed with the following sets of parameters: ($\nu_{1,max}$/kHz, ν_R/kHz, B_0/T) = (80, 62.5, 18.8); (160, 62.5, 18.8); (80, 125, 18.8) and (80, 62.5, 9.4), and the corresponding results are shown in Fig. 8a–d, respectively. These results show that D_1^K on-resonance excitation is more efficient than SLP for small and moderate C_Q values and that it is the contrary for large C_Q values. It can be seen that the efficiency of D_1^K increases: (i) with ν_1 at moderate to high C_Q value (compare Fig. 8a and b), and (ii) with ν_R and B_0 at high C_Q value (compare Fig. 8a, c and d). Indeed, a large rf field allows the use of shorter D_1^K trains, *i.e.*, smaller *K* values (compare Fig. 9a and b), which limits the losses due to H_{Q2}, which are proportional to C_Q^2. Similarly high

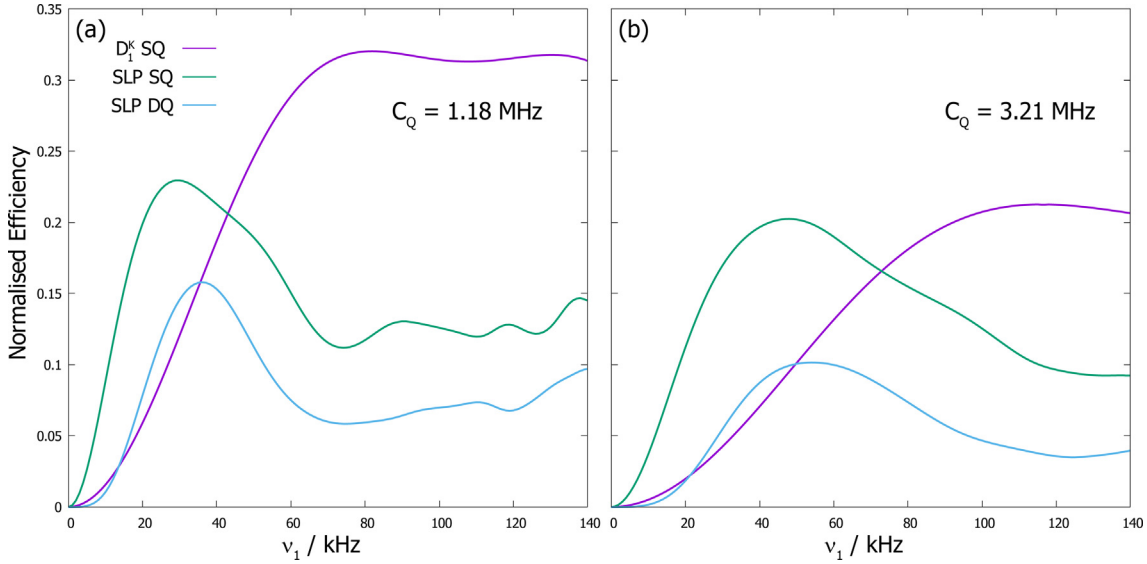

Fig. 7. Simulated on-resonance efficiency of ^{1}H-{$^{14}N^{SQ}$} and ^{1}H-{$^{14}N^{DQ}$} *J*-HMQC sequences using SLP and ^{1}H-{$^{14}N^{SQ}$} *J*-HMQC sequences using D_1^K with respect to respect to ^{14}N rf-field strength for spin systems corresponding to (a) glycine and (b) NAV. The rf-parameters (ν_1, τ_p) are indicated with + on Figs. 2–4, with D_1^5 in (a) and D_1^6 in (b).

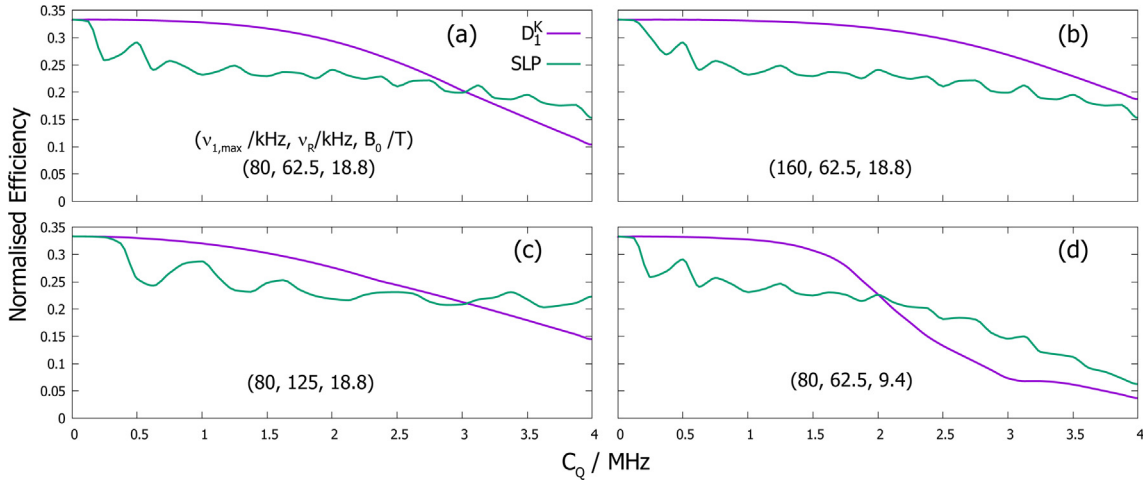

Fig. 8. Simulated on-resonance optimized efficiency of ^{1}H-{$^{14}N^{SQ}$} *J*-HMQC sequences using SLP and D_1^K (green and purple curves, respectively) for a series of quadrupole parameters corresponding to η_Q = 0.5 and C_Q = 0–4 MHz, incremented in steps of 125 kHz for ($\nu_{1,max}$/kHz, ν_R/kHz, B_0/T) = (a) (80, 62.5, 18.8); (b) (160, 62.5, 18.8); (c) (80, 125, 18.8) and (d) (80, 62.5, 9.4). For SLP, the τ_p range investigated was 1.5–2.5T_R. For D_1^K, the investigated range of the total pulse duration, $K\tau_p$, is 0–10 μs, with *K* ranging from 3 to 8, as also shown in Fig. S1 and S2. (For interpretation of the references to colour in this figure legend, the reader is referred to the web version of this article.)

MAS frequency decreases the length, KT_R, of D_1^K train, hence reducing losses due to H_{Q2}. Finally, as H_{Q2} is inversely proportional to B_0, losses produced by this interaction are smaller at high field. By contrast, the on-resonance SLP excitation exhibits very little dependence upon these parameters, and hence the range of C_Q values where D_1^K is more efficient than SLP extends with increasing ν_1, ν_R and B_0 values. However, it must be pointed out that the robustness to offset of SLP is much larger than that of D_1^K (Fig. 6), and that this robustness further increases with faster spinning speeds (Fig. 5 of [39]). Therefore, for small or moderate C_Q values, the choice in between these two schemes also depends on the range of isotropic resonance frequencies.

Fig. 9 plots the variations in optimal τ_p and *K* values of the D_1^K scheme with respect to C_Q, over the same range of parameters as for Fig. 8. These results show that, in general, to obtain a maximum efficiency with D_1^K, the higher the C_Q value, the shorter the train that should be used. Such an arrangement is effective because it limits the signal decay due to H_{Q2} dephasing [40]. This leads to a decrease of *K* with large C_Q values in Fig. 9a and d. It can be observed that, at lower B_0 field (Fig. 9d), the lengths of τ_p at high C_Q are noticeably longer than the equivalent values at 18.8 T. Long pulses allow for reduction in the length of D_1^K train, *i.e.*, the *K* value, hence limiting the losses due to H_{Q2}. Regardless of which values are used, excitation of high C_Q values at low magnetic field is likely to be inefficient with D_1^K.

It should be noted that the data presented in Figs. 8 and 9 were sorted computationally and, as such, represent theoretical, numerical maxima. These efficiencies often only differ after several decimals and so the choice between, for example, one *K* value and another, may vary from a practical perspective.

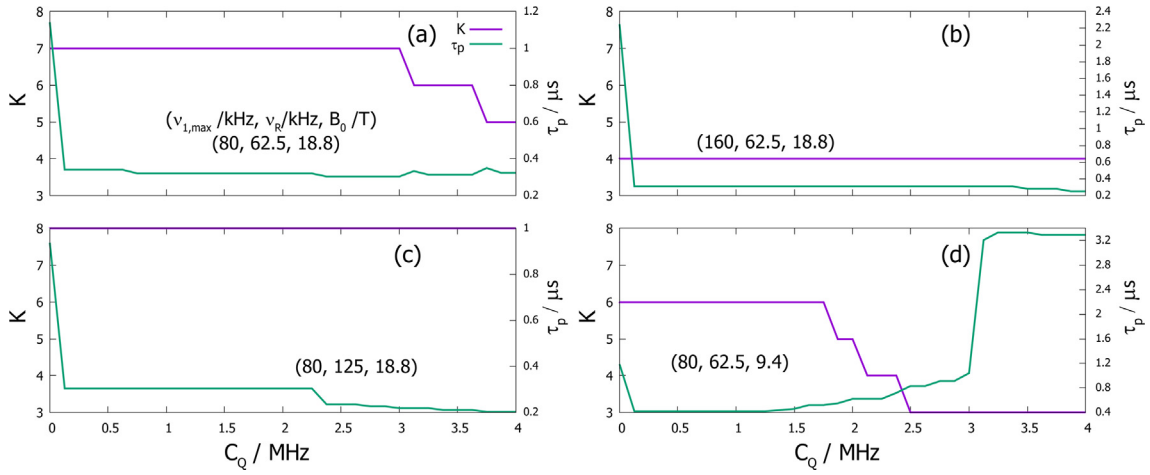

Fig. 9. τ_p and K values, green and purple curves respectively, yielding optimal simulated efficiency for ^{1}H-{^{14}N^{SQ}} J-HMQC with D_1^K for a series of quadrupole parameters corresponding to η_Q = 0.5 and C_Q = 0–4 MHz, incremented in steps of 125 kHz for ($\nu_{1,max}$/kHz, ν_R/kHz, B_0/T) = (a) (80, 62.5, 18.8); (b) (160, 62.5, 18.8); (c) (80, 125, 18.8) and (d) (80, 62.5, 9.4). (For interpretation of the references to colour in this figure legend, the reader is referred to the web version of this article.)

4. Experimental results for ^{1}H-{^{14}N} *D*-HMQC

4.1. Experimental conditions

All experiments were performed at B_0 = 18.8 T on a Bruker standard bore superconducting magnet equipped with an AV-IV console. Two model samples were selected for this study: L-histidine HCl and N-acetyl-L-valine, referred to His and NAV, and obtained from Sigma-Aldrich and Alfa Aesar, respectively, and used as-received. Their ^{1}H-{^{14}N^{SQ}} and ^{1}H-{^{14}N^{DQ}} spectra were acquired with the *D*-HMQC sequence depicted in Fig. 1b, which was employed since it is more sensitive than the *J*-HMQC variant for solids. The samples were packed into 1.3 mm rotors and spun under MAS at ν_R = 62.5 kHz, using a standard HX MAS probe. SR4$_1^2$ recoupling with $\nu_1 = 2\nu_R$ = 125 kHz was applied on ^{1}H channel during the τ_D delays to reintroduce the ^{14}N-^{1}H dipolar couplings. The ^{1}H rf-field for the $\pi/2$ and π-pulses was set to $\nu_1 \approx$ 116 kHz. The rf-field on the ^{14}N channel delivered by this probe is limited to $\nu_1 \approx$ 80 kHz. HP, D_1^K trains and SLP were employed to excite and reconvert the ^{14}N SQ or DQ coherences. The position of ^{14}N carrier frequency for His is indicated in Fig. 10. For NAV, the ^{14}N carrier frequency was resonant with the NH peak. In Fig. 12, the ^{14}N carrier frequency was varied. For 1D experiment, the t_1 delay was fixed to its minimum rotor-synchronized value equal either to $2T_R$ for rectangular pulses or KT_R for D_1^K trains. All 2D spectra were acquired using t_1 period equal to an integer multiple of T_R. This rotor-synchronization allows for refocusing of the broadening by H_{Q1} for ^{1}H-{^{14}N^{SQ}} *D*-HMQC spectra. The spectra were acquired with a relaxation delay, τ_{RD} = 1 s. The other experimental parameters are given in Table 2 as well as in the figure captions. Chemical shift referencing was carried out using solid samples of NH_4Cl (δ_{14N} = 0 ppm) and His (δ_{1H} = 8.2 ppm for N$^\tau$H). His has three ^{14}N species that possess the following NMR parameters: δ_{iso} = 4.0/146.6/133.4 ppm, C_Q = 1.26/1.46/1.29 MHz and η_Q = 0.36/0.30/0.97, for NH_3, N$^\pi$H and N$^\tau$H, respectively [58]. When taking into account their ν_{QIS} values, these peaks appear at −17200, −8500 and −9500 Hz, respectively. NAV has only one species with NMR parameters: δ_{iso} = 127.7 ppm, C_Q = 3.21 MHz and η_Q = 0.32 [51]. Its ^{14}N resonance appears at −2000 Hz on the spectra presented in this work.

4.2. Optimized parameters

In this part, we present the results observed for His and NAV that were recorded either with conventional HP (SQ, ν_1 = 80 kHz), D_1^K (SQ, ν_1 = 40 or 80 kHz) or SLP (SQ and DQ) with optimized ν_1 values. In Table 2, it can be observed that the optimized SLP length, τ_p = 20–28 µs ≈ 1.5T_R, depends very little upon the sample and hence on the C_Q value, and that these values are slightly smaller than the simulated one, $\tau_p \approx$ 32 µs = 2T_R. This small decrease is attributed to experimental losses, such as those due to ^{1}H-^{1}H dipolar couplings that were not included in the simulations. Concerning the D_1^K scheme, the pulse length with ν_1 = 80 kHz is longer than in the simulations: 1 instead of 0.6 µs for His and 0.5 instead of 0.3 µs for NAV, whereas the optimal K values are smaller: 4 instead of 5 and 6 for His and NAV, respectively. These smaller K values stem from experimental losses, such as those due to ^{1}H-^{1}H dipolar couplings, which were not included in the simulations.

4.3. Efficiencies

^{1}H-{^{14}N} *D*-HMQC spectra were acquired with the aforementioned optimized parameters from Table 2.

Fig. 10a and b demonstrate that such 2D spectra can be recorded with a good efficiency for His with experimentally achievable rf-fields of ν_1 = 80 or 40 kHz, with SQ selection and either D_1^K or SLP excitation, respectively.

The F_1 slices of the 2D spectra for NH_3, N$^\pi$H, N$^\tau$H of His and NAV, are shown in Fig. 11a–d, respectively. It can be seen that the S/N ratio observed with NAV is smaller than with His. The ^{14}N MAS linewidth of NAV is *ca.* 5–6 times larger than those of His. However, this larger indirect linewidth should not significantly affect the sensitivity because it allows for the use of fewer t_1 increments. Therefore, the main cause of the reduced HMQC efficiency in NAV is likely to be brought about by the increase in C_Q value (Fig. 8), and possibly a reduction in the ^{1}H-^{14}N dipolar coupling or ^{1}H coherence lifetime.

It is evident that, even with the highest available rf-field, HP excitation is inefficient, especially for large C_Q values, as it is the case for NAV. With respect to SQ selection, DQ always leads to a large decrease in efficiency, as previously shown *via* simulations.

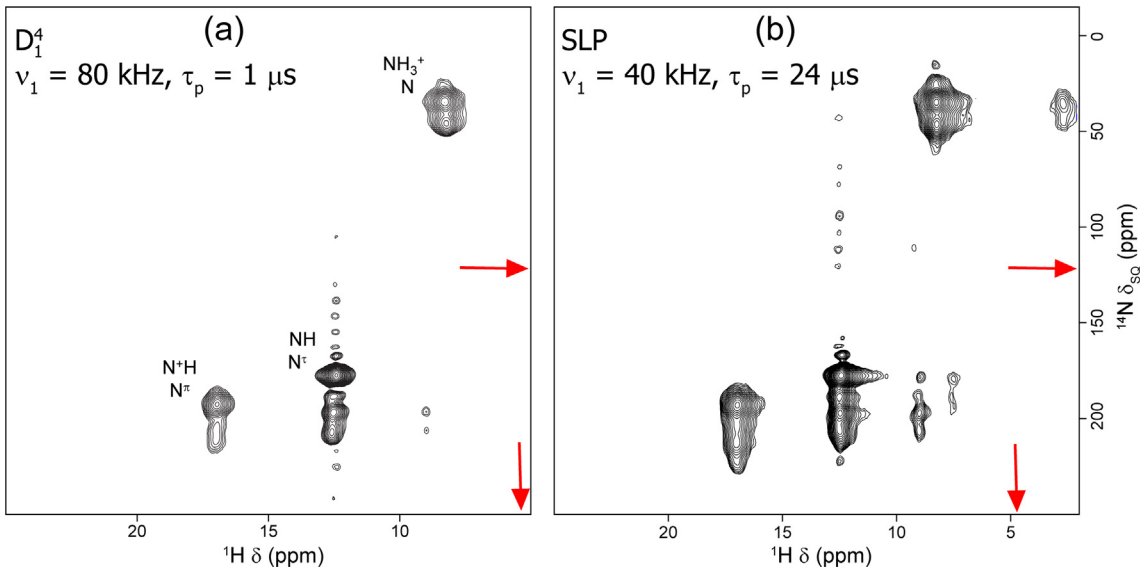

Fig. 10. ^{1}H-{^{14}N^{SQ}} *D*-HMQC spectra of His acquired using (a) D_1^4 train and (b) SLP excitation, with B_0 = 18.8 T, ν_1 = 80 (D_1^4) or 40 kHz (SLP), ν_R = 62.5 kHz. The 2D spectra result from averaging 8 transients for each of the 250 t_1 increments, resulting in a total experiment time of 33 min. Red arrows indicate the positions of the carrier frequencies. (For interpretation of the references to colour in this figure legend, the reader is referred to the web version of this article.)

Table 2
Optimal experimental parameters used for His or NAV.

Excitation	τ_D/μs	τ_p/μs	ν_1/kHz
His			
HP SQ	140	1	80
SLP SQ	140	24	40
SLP DQ	160	20	53
D_1^K SQ	140	1 (K = 6)	40
D_1^K SQ	140	1 (K = 4)	80
NAV			
HP SQ		1	80
SLP SQ	170	28	45
SLP DQ	130	28	64
D_1^K SQ	140	2 (K = 3)	40
D_1^K SQ	140	0.5 (K = 4)	80

Moreover, no resolution enhancement is observed with DQ selection over the SQ one, indicating that in the latter case the spinning speed was stable and the magic angle was well-adjusted, and hence, the broadening of SQ coherences by H_{Q1} was properly refocused. D_1^K excitation can provide almost the same level of efficiency with ν_1 = 40 or 80 kHz, because the increased value of $K\tau_p$ is able to compensate for the decrease in rf-field strength, a finding which is in agreement with previous studies [12,40]. As seen in Fig. 11a–c, the relative efficiency of SLP and D_1^K for His depends on the observed site. However, D_1^K is not efficient for large C_Q values, as shown in Fig. 11d for NAV, owing to large losses due to H_{Q2}.

4.4. Robustness to offset of SLP

Fig. 12 shows the sensitivity to ^{14}N offset observed with SLP and SQ or DQ selection, for N$^\tau$H of His (Fig. 12a and c) and NAV (Fig. 12b and d). This robustness is very large, especially with SQ selection (Fig. 12a and b), with full-width at half maximum excitation bandwidth of $S_{FWHM} \approx$ 60 and 40 kHz for His and NAV respectively, whereas it is smaller with DQ selection: $S_{FWHM} \approx$ 40 and 30 kHz (Fig. 12c and d). As previously noted, HMQC experiments using DANTE trains are less robust to offset than those using SLP, although DANTE benefits from a slight increase in overall on-resonance excitation efficiency [40]. It must be noted that the robustness to $^{14}N^{SQ}$ offset of ^{1}H-{^{14}N} *D*-HMQC 2D experiment with SLP excitation ($S_{FWHM}/\nu_R \approx$ 0.6–1.0) is much larger than that of the corresponding method with double CP MAS transfer ($S_{FWHM}/\nu_R \approx$ 0.25) (Fig. 4d-AM in [31]). It has very recently been demonstrated that optimizing the carrier frequency is recommended when using SLP and this is even more the case for D_1^K (Figs. 11 and 12 in [59]).

5. Conclusions

In this work, various previously proposed schemes for ^{14}N excitation in ^{1}H-{^{14}N} HMQC experiments have been analyzed and compared. This analysis was performed with selection of either single- (SQ) or double- (DQ) quantum levels of ^{14}N nuclei. DQ selection leads to a smaller efficiency than SQ selection, without any resolution enhancement, and is thus not generally recommended with a modern speed controller and MAS probe.

Conventional hard pulses are not efficient and should be avoided. The same recommendation is given for the XiX (X inverse X) scheme, which has recently been proposed for DQ selection.

The two most efficient methods are the sideband selective long pulse (SLP) or the D_1^K (DANTE) train of pulses. It has been shown here that SLP excitation is much more efficient than D_1^K trains for large C_Q values. As SLP is also more robust with respect to offset, rf-inhomogeneity and experimental setup, this scheme should therefore be preferred, and is particularly recommended for use by non-specialists, due to its simplicity. For weak or moderate C_Q values, the choice between the two schemes depends on the rf and magnetic field strengths, the spinning speed, and the ^{14}N isotropic frequency range. When this range is very large, SLP, which is very robust with respect to offsets, should also be the sequence of choice. In the case of paramagnetic samples, the ^{14}N isotropic shift range may even be larger than ν_R leading to folded sidebands. In this case, two 2D experiments with two different spinning speeds should be acquired in order to discriminate the center-bands from the spinning sidebands [59].

It must be emphasized that ^{1}H-{^{14}N} HMQC experiments with SQ selection, which require the cancellation of the first-order

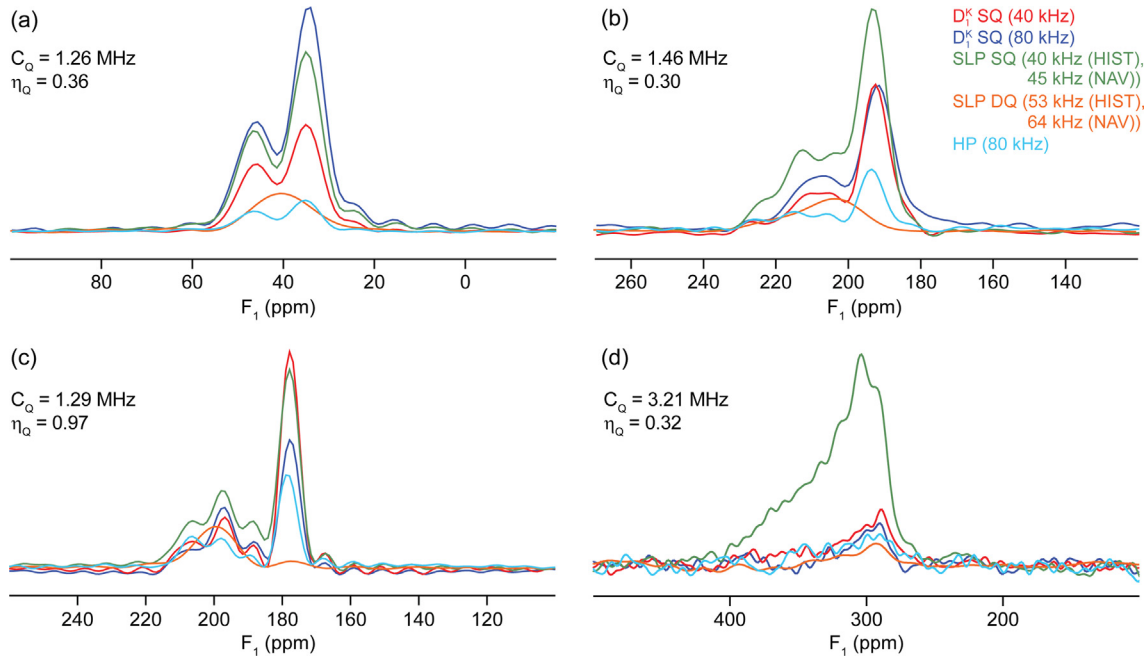

Fig. 11. F_1 slices from 2D ^{1}H-{^{14}N} *D*-HMQC spectra for (a) NH_3, (b) $N^{\pi}H$, (c) $N^{\tau}H$ of His and (d) NH of NAV, with B_0 = 18.8 T, ν_R = 62.5 kHz, and ν_1 as indicated in (b). In all cases, SQ line-shapes have been scaled up by 2 with respect to DQ ones. Additionally, the DQ ppm scale has been divided by two to allow for comparison with SQ slices. The 2D spectra result from averaging 8 (SQ) or 16 (DQ) transients for each of 250 (SQ) or 124 (DQ) t_1 increments, resulting in a total experiment time of 33 min.

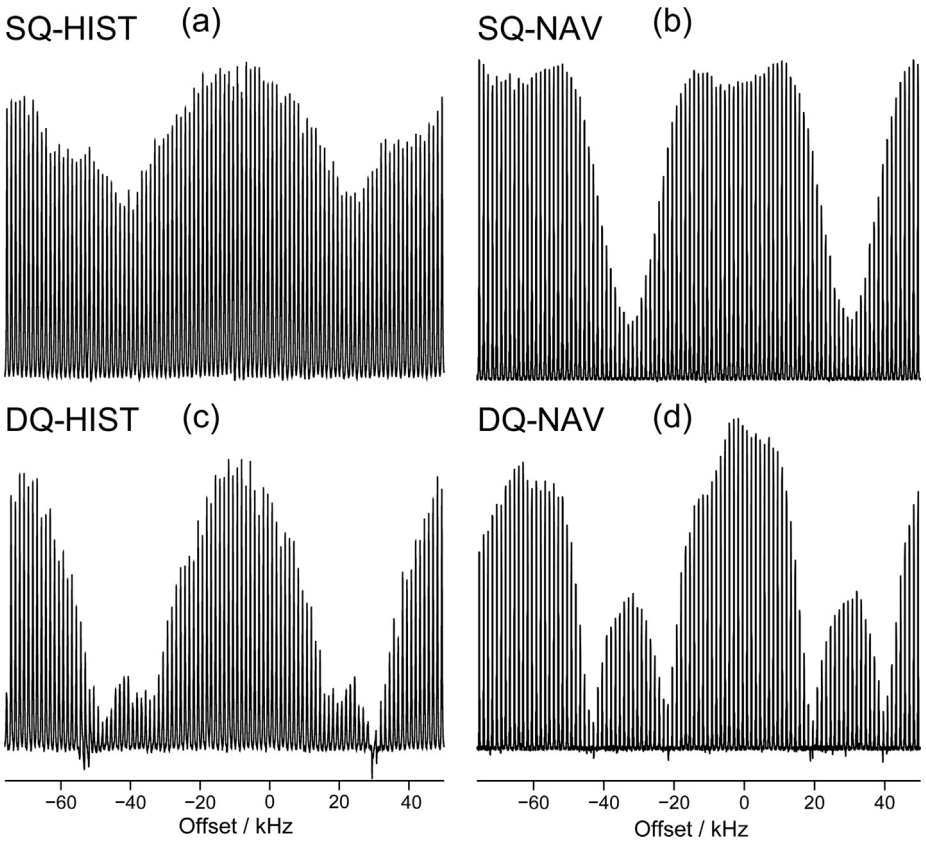

Fig. 12. Experimental (a and b) ^{1}H-{$^{14}N^{SQ}$} and (c and d) ^{1}H-{$^{14}N^{DQ}$} *D*-HMQC 1D signal *versus* ^{14}N offset with SLP of (a and c) $N^{\tau}H$ of His and (b and d) NH of NAV, at B_0 = 18.8 T with ν_R = 62.5 kHz using ν_1 = 40 (a and c) or (b and d) 45 kHz.

quadrupole dephasing in order to be well-resolved along the ^{14}N dimension, benefit from several recent technical developments. These include new MAS speed controllers that provide very stable spinning speeds, and new MAS probes with automatic magic angle adjustment with a level of precision that meets the so-called 'STMAS requirements'.

It must also be noted that very recently, a new variant of the $SR4_1^2$ recoupling sequence has been proposed for ^{1}H-{X} *D*-HMQC experiments at ultra-fast MAS. This variant replaces the basic π-pulses with $90_{-45}90_{45}90_{-45}$ composite π-pulses to decrease the effects of ^{1}H-^{1}H interactions [60]. As a result, this recoupling quenches the spin diffusion and hence long-lived coherence lifetimes can be obtained, which facilitate the detection of long N-H distances with this non-dipolar truncated sequence.

Finally, it must be noted that the ^{1}H-{^{14}N} *D*-HMQC experiment is complementary to the double CP scheme recently proposed [31]. Both methods experimentally require the same 'STMAS specifications' and ultra-fast sample spinning to minimize the losses and maximize the indirect spectral width. Compared with *D*-HMQC using SLP excitation, the double CP method exhibits a lower robustness to offset, but a better ^{14}N resolution when no ^{1}H decoupling is used. However, it should be pointed out that the ^{14}N resolution of *D*-HMQC can be enhanced with ^{1}H decoupling, and this allowed for the first detection of the cross-peak between aliphatic ^{1}H and ^{14}N ammonium site in Histidine [61]. It must also be reminded that two parameters have to be optimized with the double CP scheme: the contact times and the rf-fields to match the Hartmann-Hahn conditions [62,63], which are narrow at ultra-fast MAS [64,65]. On the contrary, there is no such rf-matching with *D*-HMQC and, moreover, with SLP excitation the ^{14}N rf-field is small and efficient over a broad range. To conclude, it ought also to be noted that the ^{1}H resolution can be enhanced by using weak continuous wave ^{14}N irradiation during t_2 [65].

Acknowledgments

Institut Chevreul (FR 2638), Ministère de l'Enseignement Supérieur et de la Recherche, Région Hauts-de-France and the European Union (FEDER/ERDF) are acknowledged for supporting and partially funding this work. Financial support from the IR-RMN-THC FR 3050 CNRS for conducting the research is gratefully acknowledged. Authors also thank ANR-17-ERC2-0022 (EOS) and ANR-18-CE08-0015-01 (ThinGlass). This project has also received funding from the European Union's Horizon 2020 research and innovation program under grant agreement no. 731019 (EUSMI). OL acknowledges financial support from Institut Universitaire de France (IUF). The computational resources were partially provided by the Polish Infrastructure for Supporting Computational Science in the European Research Space (PL-GRID). PP is grateful for funding from the MOBILITY PLUS program (grant no. DN/MOB/172/V/2017).

Appendix A. Supplementary data

Supplementary data to this article can be found online at https://doi.org/10.1016/j.jmr.2019.04.004.

References

[1] S.M. Althaus, K. Mao, J.A. Stringer, T. Kobayashi, M. Pruski, Indirectly detected heteronuclear correlation solid-state NMR spectroscopy of naturally abundant ^{15}N nuclei, Solid State Nucl. Magn. Reson. 57–58 (2014) 17–21, https://doi.org/10.1016/j.ssnmr.2013.11.001.

[2] S.L. Veinberg, K.E. Johnston, M.J. Jaroszewicz, B.M. Kispal, C.R. Mireault, T. Kobayashi, M. Pruski, R.W. Schurko, Natural abundance ^{14}N and ^{15}N solid-state NMR of pharmaceuticals and their polymorphs, Phys. Chem. Chem. Phys. 18 (2016) 17713–17730, https://doi.org/10.1039/C6CP02855A.

[3] A.J. Rossini, A. Zagdoun, M. Lelli, J. Canivet, S. Aguado, O. Ouari, P. Tordo, M. Rosay, W.E. Maas, C. Copéret, D. Farrusseng, L. Emsley, A. Lesage, Dynamic nuclear polarization enhanced solid-state NMR spectroscopy of functionalized metal-organic frameworks, Angew. Chem. Int. Ed Engl. 51 (2012) 123–127, https://doi.org/10.1002/anie.201106030.

[4] L.A. O'Dell, Direct detection of nitrogen-14 in solid-state NMR spectroscopy, Prog. Nucl. Magn. Reson. Spectrosc. 59 (2011) 295–318, https://doi.org/10.1016/j.pnmrs.2011.04.001.

[5] E. Dib, T. Mineva, B. Alonso, Chapter Three – Recent Advances in ^{14}N Solid-State NMR, in: G.A. Webb (Ed.). Annu. Rep. NMR Spectrosc. Academic Press, 2016, pp. 175–235. doi: http://doi.org/10.1016/bs.arnmr.2015.08.002.

[6] L.A. O'Dell, ^{14}N Overtone Magic Angle Spinning NMR, in: G.A. Webb (Ed.), Annu. Rep. NMR Spectrosc., Academic Press, 2015, pp. 211–236. doi: http://doi.org/10.1016/bs.arnmr.2015.04.003.

[7] J.P. Yesinowski, E.A. Hill, Wide-Line ^{14}N NMR in Solids, in: Solid-State NMR Spectrosc. Inorg. Mater., American Chemical Society, 1999, pp. 358–376. doi: http://doi.org/10.1021/bk-1999-0717.ch013.

[8] E.A. Hill, J.P. Yesinowski, Wide-line ^{14}N NMR in solids and reorientation-induced redistribution of isochromats, J. Am. Chem. Soc. 118 (1996) 6798–6799, https://doi.org/10.1021/ja960757j.

[9] L.A. O'Dell, R.W. Schurko, Fast and simple acquisition of solid-state ^{14}N NMR spectra with signal enhancement via population transfer, J. Am. Chem. Soc. 131 (2009) 6658–6659, https://doi.org/10.1021/ja901278q.

[10] V. Vitzthum, M.A. Caporini, S. Ulzega, G. Bodenhausen, Broadband excitation and indirect detection of nitrogen-14 in rotating solids using Delays Alternating with Nutation (DANTE), J. Magn. Reson. 212 (2011) 234–239, https://doi.org/10.1016/j.jmr.2011.06.013.

[11] V. Vitzthum, M.A. Caporini, S. Ulzega, J. Trébosc, O. Lafon, J.-P. Amoureux, G. Bodenhausen, Uniform broadband excitation of crystallites in rotating solids using interleaved sequences of delays alternating with nutation, J. Magn. Reson. 223 (2012) 228–236, https://doi.org/10.1016/j.jmr.2012.05.024.

[12] X. Lu, J. Trébosc, O. Lafon, D. Carnevale, S. Ulzega, G. Bodenhausen, J.-P. Amoureux, Broadband excitation in solid-state NMR using interleaved DANTE pulse trains with N pulses per rotor period, J. Magn. Reson. 236 (2013) 105–116, https://doi.org/10.1016/j.jmr.2013.09.003.

[13] K.J. Harris, S.L. Veinberg, C.R. Mireault, A. Lupulescu, L. Frydman, R.W. Schurko, Rapid acquisition of ^{14}N solid-state NMR spectra with broadband cross polarization, Chem. – Eur. J. 19 (2013) 16469–16475. doi: http://doi.org/10.1002/chem.201301862.

[14] H.J. Jakobsen, H. Bildsøe, J. Skibsted, T. Giavani, ^{14}N MAS NMR spectroscopy: the nitrate ion, J. Am. Chem. Soc. 123 (2001) 5098–5099, https://doi.org/10.1021/ja0100118.

[15] T. Giavani, H. Bildsøe, J. Skibsted, H.J. Jakobsen, A solid-state ^{14}N magic-angle spinning NMR study of some amino acids, J. Magn. Reson. 166 (2004) 262–272, https://doi.org/10.1016/j.jmr.2003.10.023.

[16] A.R. Hove, H. Bildsøe, J. Skibsted, M. Brorson, H.J. Jakobsen, Probing crystal structures and transformation reactions of ammonium molybdates by ^{14}N MAS NMR spectroscopy, Inorg. Chem. 45 (2006) 10873–10881, https://doi.org/10.1021/ic061197k.

[17] H.J. Jakobsen, A.R. Hove, H. Bildsøe, J. Skibsted, M. Brorson, Long-term stability of rotor-controlled MAS frequencies to 0.1 Hz proved by ^{14}N MAS NMR experiments and simulations., J. Magn. Reson. 185 (2007) 159–63. doi: doi://doi.org/10.1016/j.jmr.2006.12.008.

[18] M. Bloom, M.A. LeGros, Direct detection of two-quantum coherence, Can. J. Phys. 64 (1986) 1522–1528, https://doi.org/10.1139/p86-271.

[19] R. Tycko, S.J. Opella, Overtone NMR spectroscopy, J. Chem. Phys. 86 (1987) 1761–1774, https://doi.org/10.1063/1.452176.

[20] L.A. O'Dell, A. Brinkmann, ^{14}N overtone NMR spectra under magic angle spinning: Experiments and numerically exact simulations, J. Chem. Phys. 138 (2013) 64201, https://doi.org/10.1063/1.4775592.

[21] Z. Gan, I. Hung, Y. Nishiyama, J.-P. Amoureux, O. Lafon, H. Nagashima, J. Trébosc, B. Hu, ^{14}N overtone nuclear magnetic resonance of rotating solids, J. Chem. Phys. 149 (2018) 64201, https://doi.org/10.1063/1.5044653.

[22] A.J. Rossini, L. Emsley, L.A. O'Dell, Dynamic nuclear polarisation enhanced ^{14}N overtone MAS NMR spectroscopy, Phys. Chem. Chem. Phys. 16 (2014) 12890–12899, https://doi.org/10.1039/C4CP00590B.

[23] I. Haies, J.A. Jarvis, H. Bentley, I. Kuprov, P.T.F. Williamson, M. Carravetta, ^{14}N Overtone NMR under MAS: signal enhancement using symmetry-based sequences and novel simulation strategies, Phys. Chem. Chem. Phys. 17 (2015) 6577–6587, https://doi.org/10.1039/C4CP03994G.

[24] L.A. O'Dell, C.I. Ratcliffe, ^{14}N magic angle spinning overtone NMR spectra, Chem. Phys. Lett. 514 (2011) 168–173, https://doi.org/10.1016/j.cplett.2011.08.030.

[25] S. Cavadini, S. Antonijevic, A. Lupulescu, G. Bodenhausen, Indirect detection of nitrogen-14 in solids via protons by nuclear magnetic resonance spectroscopy, J. Magn. Reson. 182 (2006) 168–172, https://doi.org/10.1016/j.jmr.2006.06.003.

[26] S. Cavadini, Indirect detection of nitrogen-14 in solid-state NMR spectroscopy, Prog. Nucl. Magn. Reson. Spectrosc. 56 (2010) 46–77, https://doi.org/10.1016/j.pnmrs.2009.08.001.

[27] S.P. Brown, Nitrogen-proton correlation experiments of organic solids at natural isotopic abundance, eMagRes. 3 (2014) 243–254, https://doi.org/10.1002/9780470034590, emrstm1323.

[28] Z. Gan, J.-P. Amoureux, J. Trébosc, Proton-detected ^{14}N MAS NMR using homonuclear decoupled rotary resonance, Chem. Phys. Lett. 435 (2007) 163–169, https://doi.org/10.1016/j.cplett.2006.12.066.

[29] S. Cavadini, A. Abraham, G. Bodenhausen, Coherence transfer between spy nuclei and nitrogen-14 in solids, J. Magn. Reson. 190 (2008) 160–164, https://doi.org/10.1016/j.jmr.2007.10.008.

[30] S. Antonijevic, N. Halpern-Manners, Probing amide bond nitrogens in solids using ^{14}N NMR spectroscopy, Solid State Nucl. Magn. Reson. 33 (2008) 82–87, https://doi.org/10.1016/j.ssnmr.2008.04.006.

[31] D. Carnevale, X. Ji, G. Bodenhausen, Double cross polarization for the indirect detection of nitrogen-14 nuclei in magic angle spinning NMR spectroscopy, J. Chem. Phys. 147 (2017), https://doi.org/10.1063/1.5000689 184201.

[32] J.A. Jarvis, M. Concistre, I.M. Haies, R.W. Bounds, I. Kuprov, M. Carravetta, P.T.F. Williamson, Quantitative analysis of ^{14}N quadrupolar coupling using ^{1}H detected ^{14}N solid-state NMR, Phys. Chem. Chem. Phys. 21 (2019) 5941–5949, https://doi.org/10.1039/C8CP06276E.
[33] O. Lafon, Q. Wang, B. Hu, F. Vasconcelos, J. Trébosc, S. Cristol, F. Deng, J.-P. Amoureux, Indirect detection via spin-1/2 nuclei in solid state NMR spectroscopy: application to the observation of proximities between protons and quadrupolar nuclei, J. Phys. Chem. A. 113 (2009) 12864–12878, https://doi.org/10.1021/jp906099k.
[34] A. Brinkmann, A.P.M. Kentgens, Proton-selective ^{17}O–^{1}H distance measurements in fast magic-angle-spinning solid-state NMR spectroscopy for the determination of hydrogen bond lengths, J. Am. Chem. Soc. 128 (2006) 14758–14759, https://doi.org/10.1021/ja065415k.
[35] S. Cavadini, A. Abraham, G. Bodenhausen, Proton-detected nitrogen-14 NMR by recoupling of heteronuclear dipolar interactions using symmetry-based sequences, Chem. Phys. Lett. 445 (2007) 1–5, https://doi.org/10.1016/j.cplett.2007.07.060.
[36] Z. Gan, Measuring amide nitrogen quadrupolar coupling by high-resolution ^{14}N/^{13}C NMR correlation under magic-angle spinning, J. Am. Chem. Soc. 128 (2006) 6040–6041, https://doi.org/10.1021/ja0578597.
[37] Z. Gan, ^{13}C/^{14}N heteronuclear multiple-quantum correlation with rotary resonance and REDOR dipolar recoupling, J. Magn. Reson. 184 (2007) 39–43, https://doi.org/10.1016/j.jmr.2006.09.016.
[38] S. Cavadini, A. Lupulescu, S. Antonijevic, G. Bodenhausen, Nitrogen-14 NMR spectroscopy using residual dipolar splittings in solids, J. Am. Chem. Soc. 128 (2006) 7706–7707, https://doi.org/10.1021/ja0618898.
[39] M. Shen, J. Trébosc, O. Lafon, Z. Gan, F. Pourpoint, B. Hu, Q. Chen, J.-P. Amoureux, Solid-state NMR indirect detection of nuclei experiencing large anisotropic interactions using spinning sideband-selective pulses, Solid State Nucl. Magn. Reson. 72 (2015) 104–117, https://doi.org/10.1016/j.ssnmr.2015.09.003.
[40] Y. Li, J. Trébosc, B. Hu, M. Shen, J.-P. Amoureux, O. Lafon, Indirect detection of broad spectra in solid-state NMR using interleaved DANTE trains, J. Magn. Reson. 294 (2018) 101–114, https://doi.org/10.1016/j.jmr.2018.07.005.
[41] A.J. Pell, K.J. Sanders, S. Wegner, G. Pintacuda, C.P. Grey, Low-power broadband solid-state MAS NMR of ^{14}N, J. Chem. Phys. 146 (2017), https://doi.org/10.1063/1.4983220 194202.
[42] Y. Nishiyama, M. Malon, Z. Gan, Y. Endo, T. Nemoto, Proton – nitrogen-14 overtone two-dimensional correlation NMR spectroscopy of solid-sample at very fast magic angle sample spinning, J. Magn. Reson. 230 (2013) 160–164, https://doi.org/10.1016/j.jmr.2013.02.015.
[43] L.A. O'Dell, R. He, J. Pandohee, Identifying H-N proximities in solid-state NMR using ^{14}N overtone irradiation under fast MAS, CrystEngComm 15 (2013) 8657–8667, https://doi.org/10.1039/c3ce40967h.
[44] M. Shen, Q. Chen, J.-P. Amoureux, B. Hu, Broad-band excitation in indirectly detected ^{14}N overtone spectroscopy with composite pulses, Solid State Nucl. Magn. Reson. 78 (2016) 5–8, https://doi.org/10.1016/j.ssnmr.2016.05.001.
[45] M. Shen, J. Trébosc, L.A. O'Dell, O. Lafon, F. Pourpoint, B. Hu, Q. Chen, J.-P. Amoureux, Comparison of various NMR methods for the indirect detection of nitrogen-14 nuclei via protons in solids, J. Magn. Reson. 258 (2015) 86–95, https://doi.org/10.1016/j.jmr.2015.06.008.
[46] D. Merlet, M. Sarfati, B. Ancian, J. Courtieu, P. Lesot, Description of natural abundance deuterium 2D-NMR experiments in weakly ordered liquid-crystalline solvents using a tailored cartesian spin-operator formalism, Phys. Chem. Chem. Phys. 2 (2000) 2283–2290, https://doi.org/10.1039/B000834F.
[47] A.J. Pell, G. Pintacuda, Broadband solid-state MAS NMR of paramagnetic systems, Prog. Nucl. Magn. Reson. Spectrosc. 84–85 (2015) 33–72, https://doi.org/10.1016/j.pnmrs.2014.12.002.
[48] M. Bak, J.T. Rasmussen, N.C. Nielsen, SIMPSON: a general simulation program for solid-state NMR spectroscopy, J. Magn. Reson. 147 (2000) 296–330, https://doi.org/10.1006/jmre.2000.2179.
[49] M. Bak, N.C. Nielsen, REPULSION, a novel approach to efficient powder averaging in solid-state NMR, J. Magn. Reson. 125 (1997) 132–139, https://doi.org/10.1006/jmre.1996.1087.
[50] S.L. Veinberg, Z.W. Friedl, A.W. Lindquist, B. Kispal, K.J. Harris, L.A. O'Dell, R.W. Schurko, ^{14}N solid-state NMR spectroscopy of amino acids, ChemPhysChem 17 (2015) 4011–4027, https://doi.org/10.1002/cphc.201600873.
[51] R.E. Stark, R.A. Haberkorn, R.G. Griffin, ^{14}N NMR determination of NH bond lengths in solids, J. Chem. Phys. 68 (1978) 1996–1997, https://doi.org/10.1063/1.435879.
[52] R.A. Santos, P. Tang, W.J. Chien, S. Kwan, G.S. Harbison, NMR resolution of a crystallographic controversy: nitrogen-14 single-crystal studies of silver, barium, and lead nitrates, J. Phys. Chem. 94 (1990) 2717–2721, https://doi.org/10.1021/j100369a088.
[53] T. Giavani, H. Bildsøe, J. Skibsted, H.J. Jakobsen, Determination of nitrogen chemical shift anisotropy from the second-order cross-term in ^{14}N MAS NMR spectroscopy, Chem. Phys. Lett. 377 (2003) 426–432, https://doi.org/10.1016/S0009-2614(03)01140-0.
[54] R. Gupta, G. Hou, T. Polenova, A.J. Vega, RF inhomogeneity and how it controls CPMAS, Solid State Nucl. Magn. Reson. 72 (2015) 17–26, https://doi.org/10.1016/j.ssnmr.2015.09.005.
[55] H. Nagashima, J. Trébosc, O. Lafon, F. Pourpoint, P. Paluch, M.J. Potrzebowski, J.-P. Amoureux, Imaging the spatial distribution of radiofrequency field, sample and temperature in MAS NMR rotor, Solid State Nucl. Magn. Reson. 87 (2017) 137–142, https://doi.org/10.1016/j.ssnmr.2017.08.001.
[56] B. Dillmann, L. Dubois, E. Paleczny, J. Trébosc, J.-P. Amoureux, F. Pourpoint, O. Lafon, Local measure of the electromagnetic field in magnetic resonance coils: how do simulations help to disentangle the contributions of the electric and magnetic fields?, Solid State Nucl Magn. Reson. 82–83 (2017) 1–9, https://doi.org/10.1016/j.ssnmr.2016.12.005.
[57] Z. Tošner, A. Purea, J.O. Struppe, S. Wegner, F. Engelke, S.J. Glaser, B. Reif, Radiofrequency fields in MAS solid state NMR probes, J. Magn. Reson. 284 (2017) 20–32, https://doi.org/10.1016/j.jmr.2017.09.002.
[58] R. Siegel, J. Trébosc, J.-P. Amoureux, Z. Gan, 3D ^{1}H–^{13}C-^{14}N correlation solid-state NMR spectrum, J. Magn. Reson. 193 (2008) 321–325, https://doi.org/10.1016/j.jmr.2008.05.013.
[59] P. Paluch, A.G.M. Rankin, J. Trébosc, O. Lafon, J.-P. Amoureux, Analysis of HMQC experiments applied to a spin ½ nucleus subject to very large CSA, Solid State Nucl. Magn. Reson. 100 (2019) 11–25, https://doi.org/10.1016/j.ssnmr.2019.03.001.
[60] F.A. Perras, T.W. Goh, L.-L. Wang, W. Huang, M. Pruski, Enhanced ^{1}H-X *D*-HMQC performance through improved ^{1}H homonuclear decoupling, Solid State Nucl. Magn. Reson. 98 (2019) 12–18, https://doi.org/10.1016/j.ssnmr.2019.01.001.
[61] M. Shen, J. Trébosc, O. Lafon, F. Pourpoint, B. Hu, Q. Chen, J.-P. Amoureux, Improving the resolution in proton-detected through-space heteronuclear multiple quantum correlation NMR spectroscopy, J. Magn. Reson. 245 (2014) 38–49, https://doi.org/10.1016/j.jmr.2014.05.006.
[62] E. Stejskal, J. Schaefer, J.S. Waugh, Magic-angle spinning and polarization transfer in proton-enhanced, NMR 28 (1977) 105–112, https://doi.org/10.1016/0022-2364(77)90260-8.
[63] B.H. Meier, Cross polarization under fast magic angle spinning: thermodynamical considerations, Chem. Phys. Lett. 188 (1992) 201–207, https://doi.org/10.1016/0009-2614(92)90009-C.
[64] P. Paluch, J. Trébosc, J.-P. Amoureux, M.J. Potrzebowski, ^{1}H–^{31}P CPVC NMR method under very fast magic angle spinning for analysis of dipolar interactions and dynamics processes in the crystalline phosphonium tetrafluoroborate salts, Solid State Nucl. Magn. Reson. 87 (2017) 96–103, https://doi.org/10.1016/j.ssnmr.2017.05.004.
[65] M.K. Pandey, Y. Nishiyama, Determination of NH proton chemical shift anisotropy with ^{14}N-^{1}H heteronuclear decoupling using ultrafast magic angle spinning solid-state NMR, J. Magn. Reson. 261 (2015) 133–140, https://doi.org/10.1016/j.jmr.2015.10.015.